Cellular/Molecular

Sharp Ca^{2+} Nanodomains beneath the Ribbon Promote Highly Synchronous Multivesicular Release at Hair Cell Synapses

Cole W. Graydon,[1,2]* Soyoun Cho,[3]* Geng-Lin Li,[3] Bechara Kachar,[1] and Henrique von Gersdorff[3]

[1]National Institute on Deafness and Other Communication Disorders, National Institutes of Health, Bethesda, Maryland 20892, [2]Brown–NIH Graduate Partnerships Program, Department of Neuroscience, Brown University, Providence, Rhode Island 02906, and [3]The Vollum Institute, Oregon Health & Science University, Portland, Oregon 97239

Hair cell ribbon synapses exhibit several distinguishing features. Structurally, a dense body, or ribbon, is anchored to the presynaptic membrane and tethers synaptic vesicles; functionally, neurotransmitter release is dominated by large EPSC events produced by seemingly synchronous multivesicular release. However, the specific role of the synaptic ribbon in promoting this form of release remains elusive. Using complete ultrastructural reconstructions and capacitance measurements of bullfrog amphibian papilla hair cells dialyzed with high concentrations of a slow Ca^{2+} buffer (10 mM EGTA), we found that the number of synaptic vesicles at the base of the ribbon correlated closely to those vesicles that released most rapidly and efficiently, while the rest of the ribbon-tethered vesicles correlated to a second, slower pool of vesicles. Combined with the persistence of multivesicular release in extreme Ca^{2+} buffering conditions (10 mM BAPTA), our data argue against the Ca^{2+}-dependent compound fusion of ribbon-tethered vesicles at hair cell synapses. Moreover, during hair cell depolarization, our results suggest that elevated Ca^{2+} levels enhance vesicle pool replenishment rates. Finally, using Ca^{2+} diffusion simulations, we propose that the ribbon and its vesicles define a small cytoplasmic volume where Ca^{2+} buffer is saturated, despite 10 mM BAPTA conditions. This local buffer saturation permits fast and large Ca^{2+} rises near release sites beneath the synaptic ribbon that can trigger multiquantal EPSCs. We conclude that, by restricting the available presynaptic volume, the ribbon may be creating conditions for the synchronous release of a small cohort of docked vesicles.

Introduction

At hair cell afferent synapses, a synaptic ribbon is affiliated with the sites of Ca^{2+} channel clustering and exocytosis (Zenisek et al., 2004; Frank et al., 2010). The ribbon tethers a shell of synaptic vesicles, a small subset of which dock onto, or reside very close to, the presynaptic membrane. Remarkably, hair cell ribbon synapses can sustain high release rates of several hundred vesicles per second over prolonged periods (Parsons et al., 1994). This seemingly inexhaustible supply of vesicles is presumed to result from a vigorous replenishment of the ribbon-associated vesicles by the multitude of vesicles that populate the surrounding cytoplasm. Mechanisms for signaling, transporting, and mobilizing these vesicles remain unclear, although vesicle pool replenishment is influenced by Ca^{2+} and depends on a Ca^{2+}-sensor protein unique to hair cells called otoferlin (Roux et al., 2006; Johnson et al., 2008; Pangrsic et al., 2010).

Another hallmark of ribbon function is multivesicular release, in which more than one vesicle fuses at a single synapse to produce EPSCs that are much larger than mEPSCs (Glowatzki and Fuchs, 2002; Grant et al., 2010). In frog hair cells, a transition from mEPSCs to predominantly large EPSCs occurs with a small difference in presynaptic membrane potential of only a few millivolts (Li et al., 2009), suggesting that this transition occurs with the incremental opening of a few Ca^{2+} channels per synapse (Brandt et al., 2005; Jarsky et al., 2010). Two leading hypotheses have been proposed to explain multivesicular release. One involves the homotypic fusion of vesicles (so called, compound fusion) (Matthews and Sterling, 2008); the other, the coordinated fusions of several docked vesicles at the plasma membrane (Singer et al., 2004). However, both explanations are confounded by the fact that multivesicular release remains robust even upon the introduction of strong presynaptic Ca^{2+} buffering (Goutman and Glowatzki, 2007), which is estimated to restrict the mean distance of free Ca^{2+} diffusion to $<$10 nm from the pore of the Ca^{2+} channel for 10 mM BAPTA (Bucurenciu et al., 2008; Parekh, 2008). In the context of these tight spatial constraints, the large size of some multivesicular EPSCs (composed of five or more vesicles) is baffling, especially considering the low Ca^{2+}

Received April 13, 2011; revised Sept. 15, 2011; accepted Sept. 25, 2011.

Author contributions: C.W.G., S.C., G.-L.L., B.K., and H.v.G. designed research; C.W.G., S.C., and G.-L.L. performed research; C.W.G., S.C., G.-L.L., B.K., and H.v.G. analyzed data; C.W.G., S.C., G.-L.L., B.K., and H.v.G. wrote the paper.

This work was supported by NIDCD Grant DC04274 (H.v.G.), a Deafness Research Foundation Grant and a Tartar Fellowship (S.C.), a K99 Research Award from NIDCD (G.-L.L.), and the NIDCD Division of Intramural Research (C.W.G., B.K.). We thank Will Grimes and Gary Matthews for discussions.

*C.W.G. and S.C. contributed equally to this work.

Correspondence should be addressed to either of the following: Bechara Kachar, National Institute on Deafness and Other Communication Disorders, National Institutes of Health, 50 South Drive, MSC 8027, Bethesda, MD 20892-8027, E-mail: kacharb@nidcd.nih.gov; or Henrique von Gersdorff, The Vollum Institute, Oregon Health & Science University, 3181 Southwest Sam Jackson Park Road, Portland, OR 97239, E-mail: vongersd@ohsu.edu.

DOI:10.1523/JNEUROSCI.1866-11.2011

 0270-6474/11/3116637-14$15.00/0

sensitivity of the release machinery of the hair cell (Beutner et al., 2001).

The complex relationship between vesicle populations and Ca^{2+} influx into the crowded presynaptic space under a synaptic ribbon has yet to be fully characterized. Here, we combine electrophysiology with a thorough ultrastructural analysis to determine the size of morphologically and functionally defined vesicle pools at an adult hair cell synapse. We find that a slow Ca^{2+} buffer (10 mM EGTA) can decrease vesicle recruitment rates and thus uncovers the size of two distinct vesicle pools. Furthermore, by incorporating our ultrastructural findings into Monte Carlo simulations of Ca^{2+} influx at ribbon-type active zones, we suggest that volume exclusion by the presence of the ribbon and its associated vesicles can produce a sharp local Ca^{2+} rise and account for the observed characteristics of multivesicular release at auditory hair cell synapses.

Materials and Methods

Tissue and hair cell preparation. All procedures followed the Oregon Health & Sciences University or National Institutes of Health (protocol 1215-08) approved animal care protocols and guidelines. For physiology studies, adult bullfrogs (*Rana catesbeiana*) of either sex were sedated by placing them in an ice bath for ~20 min, and then double-pithed and decapitated. Amphibian papillae were carefully dissected from the frog's ear. To expose hair cells and afferent fibers for patch clamping, amphibian papilla were stretched out and split with fine microtools in a recording chamber with oxygenated artificial perilymph (Keen and Hudspeth, 2006; Li et al., 2009). Artificial perilymph contained the following (in mM): 95 NaCl, 2 KCl, 2 $CaCl_2$, 1 $MgCl_2$, 25 $NaHCO_3$, 3 glucose, 1 creatine, 1 sodium pyruvate, pH adjusted to 7.3, and bubbled with 95% O_2 and 5% CO_2. Salts and chemicals were bought from Sigma-Aldrich or from Ascent. During the recordings, the preparation was perfused continuously (2–3 ml/min) with oxygenated artificial perilymph.

Electrophysiology. Preparations were viewed with an Olympus BX51WI or Zeiss Axioscope II FS microscope equipped with a 40 or 60× water-immersion objective and a CCD camera (XC-75; Sony) with contrast enhancement (C2741; Hamamatsu). Whole-cell recordings were performed with a double EPC-9/2 or EPC-10/2 (HEKA Elektronik) patch-clamp amplifier and Pulse software (HEKA) at room temperature. Patch pipettes of borosilicate glass (World Precision Instruments) were pulled to resistances of 5–6 MΩ for hair cells and 8–10 MΩ for afferent fibers with a Narishige model PP-830 puller or a Sutter model P-97 puller. The standard internal solution contained the following (in mM): 77 Cs-gluconate, 20 CsCl, 1 $MgCl_2$, 10 TEA (tetraethylammonium)-Cl, 10 HEPES, 2 EGTA, 3 Mg-ATP, 1 Na-GTP, and 5 Na_2-phosphocreatine, adjusted to pH 7.3 with CsOH. The averaged uncompensated series resistances (R_s) in whole-cell recordings were 13.2 ± 0.4 MΩ for 27 hair cell recordings and 31 ± 9 MΩ for 15 afferent-fiber recordings. We did not use electronic series resistance compensation for most of the fiber recordings because this added noise and often resulted in ringing and the loss of the recording. Errors in the voltage command due to uncompensated series resistance were not corrected off-line. In five afferent fibers held at −90 mV, we recorded spontaneous EPSCs before and after 50–70% series resistance compensation. No significant changes were observed for peak amplitudes (124 ± 34 vs 159 ± 54 pA), charge transferred (152 ± 58 vs 170 ± 69 fC), or for 10–90% rise time (0.27 ± 0.01 vs 0.26 ± 0.02 ms; $n = 5$). Hair cells and afferent fibers were held at −90 mV after being corrected for liquid junction potentials. The current signal was low-pass filtered at 2 kHz and sampled at 20 kHz or higher.

Capacitance measurements. Whole-cell membrane capacitance (C_m) was measured from hair cells under voltage clamp with the "Sine + DC" method (Lindau and Neher, 1988) using a double EPC9/2 amplifier and Pulse software. Patch pipettes were coated with dental wax (Cavex) to minimize noise and pipette capacitance. A 1 kHz sine wave (50 mV peak-to-peak) was superposed on the holding potential of the hair cells of −90 mV, and the resulting current was used to calculate C_m via the Pulse software emulator of a lock-in amplifier (Gillis, 2000). The change of capacitance, $\Delta C_m = C_{m\ (response)} - C_{m\ (baseline)}$, was used as a proxy of total synaptic vesicle exocytosis from a single hair cell. An average of $C_{m\ (response)}$ and $C_{m\ (baseline)}$ was obtained by averaging C_m data points before and after the depolarizing pulse. Data analysis was performed with IGOR Pro software (Wavemetrics) and Prism (GraphPad Software).

Resonant frequencies of hair cells. To measure the resonant frequency, we injected step current into the hair cells and measured the resulting membrane potential oscillations. These membrane potential oscillations decayed exponentially in amplitude and reached a steady-state membrane potential (V_{ss}). To calculate the resonant frequency (f_c), we fit the current-clamp data points using the following equation: $V(t) = A \cdot \sin(2\pi \cdot f_c \cdot (t - t_0) + \phi) \cdot \exp[-(t - t_0)/\tau] + V_{ss}$, where A is the amplitude of voltage oscillation, ϕ is the phase, and τ is the single exponential decay time constant (Crawford and Fettiplace, 1981).

Noise analysis on Ca^{2+} tail currents. Nonstationary noise analysis of Ca^{2+} currents was used to estimate the number of Ca^{2+} channels per hair cell and their single-channel current (Roberts et al., 1990). To obtain a complete relationship between the mean and variance of the Ca^{2+} currents for low- and high-amplitude Ca^{2+} currents, we included 5 μM 1,4-dihydro-2,6-dimethyl-5-nitro-4-[2-(trifluoromethyl)phenyl]-3-pyridinecarboxylic acid, methyl ester (BayK 8644), in the bath solution to maximize the open probability of the L-type Ca^{2+} channels of the hair cell (Fox et al., 1987). To keep resting Ca^{2+} levels very low, hair cells were first held at −90 mV, and then stepped to −110 mV to relieve Ca^{2+} channels from any Ca^{2+} or voltage-dependent inactivation. This was followed by a step depolarization to +30 mV, opening all (or nearly all) of the Ca^{2+} channels. A membrane voltage step back to −90 mV produced a large and sudden increase of driving force. As a result, a large Ca^{2+} tail current was elicited through the open channels, which decreased quickly as the Ca^{2+} channels reclosed (see Fig. 6*B*). For each hair cell, we collected a total of 100 leak-subtracted current traces (elicited every 100 ms), and the mean and variance of these currents were calculated point-by-point using a custom-made IGOR Pro analysis program. After plotting the variance against the mean current, the data were fit to a parabolic function: $\mathrm{Var}(I) = i \cdot I - I^2/N_{Ca} + E_{noise}$, where I is the mean current, i is the single-channel current, E_{noise} is the electrical noise, and N_{Ca} is the number of Ca^{2+} channels.

Serial section reconstructions. For electron microscopy, bullfrogs were anesthetized by intraperitoneal injection of a buffered solution of MS-222 (ethyl 3-aminobenzoate methanesulfonic acid) followed by double-pithing and decapitation. Under a dissecting scope, the entire bullfrog inner ear was excised from the surrounding bone and fixed immediately by immersion in 2.5% glutaraldehyde/2% paraformaldehyde/3 mM $CaCl_2$/0.1 M cacodylate buffer, pH 7.3. Alternatively, some bullfrog tissue ("zero-calcium" condition) was incubated for 10 min in a Ca^{2+}-free frog Ringer's (in mM: 110 Na, 2 K, 3 Mg, 1 EGTA, 5 HEPES, 118 Cl, 3 D-glucose, 1 pyruvate, 1 creatine; pH 7.3) before fixation in 2.5% glutaraldehyde/2% paraformaldehyde/0.1 M cacodylate buffer, pH 7.3. After fixing, the tissue was postfixed in 1% osmium tetroxide in 0.1 M cacodylate buffer, pH 7.3, for 1 h. For some preparations, the tissue was then stained *en bloc* with 2% aqueous uranyl acetate for 1 h. The tissue was washed with dH_2O, dehydrated in a graded series of acetone or PPO [poly(*p*-phenylene oxide)], and embedded in EMbed 812 resin (Electron Microscopy Sciences).

For whole-cell reconstructions, sets of 150-nm-thick serial sections (typically 150–200 sections per set) were collected on 2 × 1 mm single-slot grids coated with Formvar. The sets were then imaged in a JEOL 1010 electron microscope operating at 80 kV at a magnification of 2500×. Overlapping images were taken of each section and later montaged in either Reconstruct (Fiala, 2005) or Adobe Photoshop CS3 (Adobe Systems). From this data set, we quantified the number, diameter, and spacing of all the synaptic ribbons and mapped their afferent fiber connectivity. The number of ribbons per hair cell was either counted directly from four hair cells that were entirely reconstructed, or extrapolated for the hair cells that were reconstructed halfway through their longitudinal diameter (using ~53 consecutive sections, or ~8 μm).

Determination of vesicle pool sizes from serial sections. For single-ribbon synapse reconstructions, serial 50-nm-thick sections were collected on grids and imaged at 40,000× as described above. Alignment, reconstruc-

tions, and morphometric analysis were made in Reconstruct software. We used second-order polynomial fits to describe the relationship between ribbon diameters and the number of associated synaptic vesicles. For each ribbon, we counted the number of synaptic vesicles that were within 30 nm from the ribbon surface—this represented the ribbon-attached vesicle pool (RAP). A subset of the ribbon-attached vesicles, where the distance of the vesicle was within <20 nm from the presynaptic membrane, was considered the docked pool or the immediately releasable pool (IRP)—the presumed pool of vesicles that release first during a depolarization (Lenzi et al., 1999; Schnee et al., 2011). The value of 20 nm was chosen because t-SNARE and v-SNARE proteins have a cytosolic length of ~10 nm, so SNARE interactions may occur from a distance of 20 nm from the presynaptic plasma membrane (Zenisek et al., 2000; Castorph et al., 2010). By combining our whole-cell reconstruction data with our individual ribbon reconstruction data and taking into account the ribbon size distribution, we estimated the total size of the RAP and IRP per hair cell.

Synaptic vesicle size distributions. The diameters of vesicles in the RAP were calculated in our serial sections by drawing a best-fit ellipse over each synaptic vesicle membrane through the center of the lipid bilayer. The diameters of each vesicle profile, approximated as a circle, were then calculated from the area of each ellipse.

Tomographic reconstructions. Plastic sections (200 nm) taken from the preparations described above were collected on hex mesh grids. Colloidal gold (10 nm; Sigma-Aldrich) was applied to both sides of the sections to act as fiducial markers before imaging with a Zeiss 922 transmission electron microscope operating at 160 kV and equipped with a 2k Gatan CCD camera and Digital Micrograph (Gatan) tomography acquisition software. Tilt series (from −65 to +65°) images were acquired at magnifications producing image pixel sizes ranging from 0.7 to 1.4 nm. Images were aligned with IMOD software (Kremer et al., 1996), reconstructed using EM3D software (Ress et al., 1999), and then rendered, segmented, and analyzed using Reconstruct software.

Determination of vesicle pool sizes from tomographic reconstructions. To estimate vesicle pools in our tomographic reconstructions of ribbon synapses, we used only data sets that included the center of the ribbon. Because ribbons were approximately spherical, for each data set we measured the largest cross-sectional area of the ribbon to estimate a corresponding ribbon diameter value. Ribbon-attached vesicles formed a shell enclosing the ribbon, so vesicle pool estimates were made based on the percentage of the vesicle shell reconstructed. The diameter of this shell incorporated the diameter of the ribbon, one-half the diameter of attached vesicles, and the length (mean length ± SD, 30.2 ± 6.0; $n = 10$) of the filamentous tether attaching the vesicle to the ribbon measured from the tomographic reconstructions. For these reconstructions, we defined the IRP in the same way as in the serial section reconstructions. We also counted vesicles associated with the ribbon and touching the presynaptic membrane, a feature strictly discernible only by using electron tomography (Lenzi et al., 2002).

Monte Carlo modeling. All simulations were done using MCell 3 software (Stiles et al., 1996; Stiles and Bartol, 2001) and included 3D models generated in the open-source program Blender (www.blender.org) (Czech et al., 2009). Results from these simulations were analyzed using Excel (Microsoft) and IGOR Pro software. Model parameters were sourced from our ribbon synapse reconstructions. Specifically, a model of a 200 nm, spherical ribbon was placed opposing a presynaptic membrane that contoured the base of the ribbon. A shell of 78 total vesicles (35 nm outer diameter) was added 30 nm from the edge of the ribbon to account for the length of the tether. The ribbon and vesicles were considered to be reflective to Ca^{2+}, unbound buffer, and bound buffer. At the base of the ribbon, 14 (see Fig. 7) or 15 (see Fig. 8) of the vesicles were clustered in the 37 nm gap between the ribbon and presynaptic membrane. A total of 45 Ca^{2+} channels were randomly tiled underneath the ribbon on two stripes of presynaptic membrane (33 × 100 nm) spaced 50 nm apart, consistent with previous accounts of channel arrangement at ribbon synapses (Roberts et al., 1990; Frank et al., 2010). Each open channel was given a Ca^{2+} current consistent with our noise analysis estimates (see Fig. 6). Because local free Ca^{2+} concentrations stabilized within 1–2 ms after channels opened, stochastic timing of channel openings and closings was simplified: channels opened together and remained open for the duration of the simulation. A box (400 × 400 × 300 nm) enclosed the entire model. The walls of the box released unbound buffer in proportion to Ca^{2+} influx from the channels, effectively "clamping" its concentration in the simulation. The box walls absorbed both free Ca^{2+} and bound buffer. The diffusion coefficients for free Ca^{2+} (D_{Ca} = 200 $\mu m^2 s^{-1}$) and for Ca^{2+} buffer (bound or unbound, D_{Bu} = 20 $\mu m^2 s^{-1}$) are the same as those used in a previous study (Roberts, 1994). The time step used in the simulations (30 ns) resulted in average diffusion lengths per time step of 5.5 nm for Ca^{2+} and 1.7 nm for buffer. Our buffer Ca^{2+} binding rates (k_{ON} = 9.6 $\mu M^{-1} s^{-1}$ and k_{OFF} = 0.86 s^{-1}; or k_{ON} = 500 $\mu M^{-1} s^{-1}$ and k_{OFF} = 96 s^{-1}) were chosen to reflect EGTA and BAPTA, respectively (Bortolozzi et al., 2008). Unbound buffer was allowed to equilibrate to a uniform concentration before Ca^{2+} channels were opened. At eight locations, progressively distant from the base of the ribbon, 10 nm boxes were incorporated into the simulation to monitor (in 50 μs increments) the concentrations of buffer and free Ca^{2+} following the opening of channels (see Fig. 7*A*).

Results

Multiquantal EPSCs evoked under strong Ca^{2+} buffering are highly synchronous

For this comparative physiology and ultrastructure study of auditory hair cell ribbon synapses, we used hair cells and afferent fibers in the midfrequency (350–550 Hz) region of bullfrog amphibian papillae (Fig. 1*A*, dashed line) (Lewis et al., 1982). *In vivo* recordings of turtle and frog auditory hair cells have described resting membrane potentials in the range of −55 to −50 mV (Crawford and Fettiplace, 1980; Pitchford and Ashmore, 1987). In five paired recordings in which our hair cells were depolarized to −54 mV, large amplitude EPSC events were observed in the afferent fiber even though the hair cell was dialyzed with a high concentration of a fast Ca^{2+} buffer (10 mM BAPTA; Fig. 1*B*). These large events occurred in a stochastic manner during the depolarization, but were absent when the hair cell potential was held at −90 mV. In previous studies, this concentration of BAPTA completely blocked release from the ribbon-type synapses of retinal bipolar cells even after strong depolarizations (von Gersdorff and Matthews, 1994; Coggins and Zenisek, 2009). How does the hair cell release machinery overcome this strong Ca^{2+} buffering?

By drastically limiting the spread of Ca^{2+} into the terminal, fast and strong Ca^{2+} buffering might change the exact timing of exocytosis and, as a result, alter the kinetics of individual EPSC events. However, the individual EPSC events of Figure 1*B* were monophasic with a sharp rise and decay time course, having the same kinetics as small mEPSCs (Fig. 1*C*), and the majority of the release events had large amplitudes (mean amplitude, −203 pA; Fig. 1*D*). This indicated that the EPSCs were multiquantal, with a quantal content of four to six vesicles, given that the average quantal size is −57 pA at an afferent fiber holding potential of −90 mV (Li et al., 2009). To determine whether Ca^{2+} buffering alters hair cell release kinetics by desynchronizing multiquantal release, we analyzed the kinetics of individual EPSCs obtained under several different conditions: first, with 2 mM EGTA or 10 mM BAPTA (both done with paired recordings), and second, when the hair cell was unperturbed (afferent fiber recordings of spontaneous EPSCs). With an internal solution containing 2 mM EGTA, multivesicular release began to occur for hair cell potentials more depolarized than −70 mV (Li et al., 2009). Small events (uniquantal: 0 ~ −100 pA) and large events (multiquantal: −100 ~ −200 pA) had similar 10~90% rise time (0.26 ± 0.06 vs 0.27 ± 0.03 ms; $n = 5$ pairs; $p > 0.05$ for paired Student's t test) and similar exponential decay time constants (0.62 ± 0.17 vs

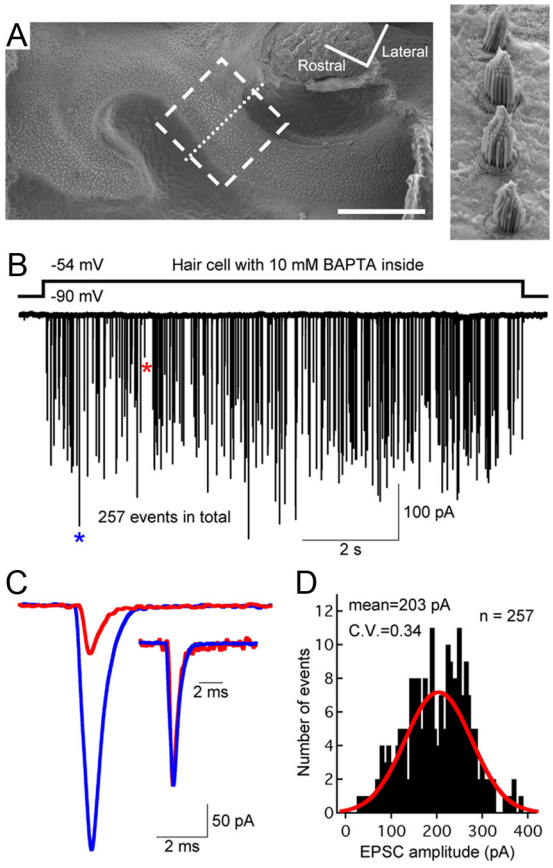

Figure 1. Hair cells from the bullfrog amphibian papilla: a step depolarization evokes multivesicular EPSCs even when the hair cell is dialyzed with 10 mM BAPTA. ***A***, Scanning electron micrograph of the amphibian papilla surface, showing the 400–500 Hz region where electrophysiological recordings and morphological reconstructions were performed (dashed box). The higher magnification image (right) shows hair bundles from hair cells along the dotted line. Scale bar: 200 μm. ***B***, Paired recordings of a single 10 mM BAPTA dialyzed hair cell and its connected afferent fiber show that a step depolarization of the hair cell from −90 to −54 mV was sufficient to evoke large-amplitude EPSCs that occurred stochastically during the depolarizing pulse. ***C***, A large-amplitude EPSC (blue star) and a small-amplitude EPSC (red star) from ***B*** are superimposed and shown at high temporal resolution. The two EPSCs have similar waveforms after normalization to the same peak value (inset). ***D***, Amplitude distribution of all EPSCs shown in ***B*** (bin size, 5 pA). The distribution can be fit with a Gaussian function (red) and has an average amplitude of 203 pA ($n = 257$ EPSCs), corresponding to a quantal content of approximately four to five quanta (or released vesicles).

0.63 ± 0.16 ms; $n = 5$ pairs; $p > 0.05$ for paired Student's t test). For an internal solution containing 10 mM BAPTA multivesicular release began to occur only for hair cell potentials more depolarized than −60 mV (Li et al., 2009). Once again, the small events and large events had similar waveforms (0.27 ± 0.04 vs 0.26 ± 0.02 ms for 10∼90% rise time; 0.50 ± 0.05 vs 0.53 ± 0.06 ms for decay time constant; $n = 5$; $p > 0.05$ for paired Student's t test). Statistical analysis for EPSC events with 2 mM EGTA versus 10 mM BAPTA revealed no significant change of 10∼90% rise time or decay time constant for either small or large events ($p > 0.05$ for unpaired Student's t test). For spontaneous EPSCs, in which the hair cell was not patch clamped, small events had a 10–90% rise time of 0.30 ± 0.06 ms and a decay time constant of 0.58 ± 0.05 ms, which was not significantly different from large events (0.27 ± 0.04 ms rise time, and 0.56 ± 0.05 ms decay; $n = 6$; $p > 0.05$ for paired Student's t test). Therefore, the kinetics of individual afferent fiber EPSCs appears to be remarkably insensitive to the strength of Ca^{2+} buffering in the hair cell.

Vesicle pool sizes determined with 10 mM EGTA

Because strong Ca^{2+} buffering conditions in the hair cell are unable to desynchronize the large multivesicular EPSC events, multivesicular release may be mediated by a subpopulation of vesicles tightly coupled (within a few nanometers) to Ca^{2+} channels. To determine the size of synaptic vesicle pools and the maximal rates of exocytosis, we used strongly depolarizing pulses from −90 to −30 mV (the peak of Ca^{2+} current) and measured changes in the membrane capacitance (ΔC_m) of the hair cell (Parsons et al., 1994; von Gersdorff and Matthews, 1994; Hallermann et al., 2003). The durations of the depolarizing pulses were varied so that we could determine vesicle pool sizes by the saturation of ΔC_m increases. Different intracellular Ca^{2+} buffers were also used to better isolate plateaus in C_m changes. The ΔC_m jumps obtained with either 2 mM EGTA (Fig. 2*A*) or 10 mM BAPTA (Fig. 2*B*) were dramatically different in size (note the fivefold difference in vertical scale). For example, the ΔC_m evoked by a short 100 ms pulse with 2 mM EGTA was 60 ± 4 fF ($n = 26$), which was not significantly different from the ΔC_m = 74 ± 11 fF ($n = 16$; $p = 0.16$) evoked by a 3-s-long pulse with 10 mM BAPTA. Despite the effectiveness of BAPTA at blocking most of the exocytosis evoked by prolonged 1- to 3-s-long depolarizing pulses, a small amount of exocytosis (∼10%) was resistant, consistent with the EPSC data of Figure 1*B*. Fast Ca^{2+} current inactivation was consistently observed immediately after the initial current peak for hair cells held at −90 mV (Cho et al., 2011), and was followed by a slow form of Ca^{2+}-dependent inactivation, more pronounced with EGTA than BAPTA, as has been described at turtle auditory hair cells (Schnee and Ricci, 2003) (Fig. 2*A*).

Averaging ΔC_m across cell populations might introduce systematic errors due to the variation in cell sizes because cells of different sizes may contain different numbers and types of synaptic ribbons (von Gersdorff et al., 1996; Martinez-Dunst et al., 1997). We next checked whether the size of the hair cell was correlated with the total amount of exocytosis. We plotted ΔC_m evoked by 20-ms-long [$n = 16$; coefficient of variation (CV) = 0.34)], 100-ms-long ($n = 17$; CV = 0.20), and 500-ms-long ($n = 22$; CV = 0.22) pulses against the resting C_m of each cell, which varied from 10 to 14.8 pF. However, regardless of pulse duration, the resting C_m was very weakly correlated with ΔC_m (data not shown), justifying our calculations of average ΔC_m across hair cells in the midfrequency range of amphibian papilla (Smotherman and Narins, 2000).

A plot of average ΔC_m against pulse duration for the 2 mM EGTA data revealed three distinct kinetic subgroups (Fig. 3*A*,*B*): the first from 2 to 50 ms (Fig. 3*B*, left), the second from 100 ms to 1 s (Fig. 3*B*, middle), and the third from 1 to 3 s (Fig. 3*B*, right). The data from each of these groups were well described by a linear function ($R^2 \geq 0.97$; Fig. 3*B*, black dashed lines). The slope of the linear fit in the first subgroup (slope, 0.8 fF/ms) was the steepest, the second subgroup had a smaller slope (=0.2 fF/ms), and the third subgroup showed the least slope (=0.1 fF/ms), suggesting that transmitter release kinetics evoked by short pulses were eightfold faster than those by longer pulses. However, the capacity for fast exocytosis lasted only for ∼50 ms, whereas the slower forms of exocytosis could be sustained for longer periods. In contrast, plotting ΔC_m against total Ca^{2+} charge (the integral of Ca^{2+} currents after leak subtraction) revealed only two distinct subgroups (Fig. 3*C*), although the relationship between ΔC_m and Ca^{2+} charge in both subgroups was again well described by a linear fit ($R^2 \geq 0.98$; Fig. 3*C*, lines). The first group ranged from 2 to 50 ms (Fig. 3*C*, no. 1), while the second group ranged from 100 ms to 3 s (Fig. 3*C*, no. 2). Assuming that the rate of exocytosis

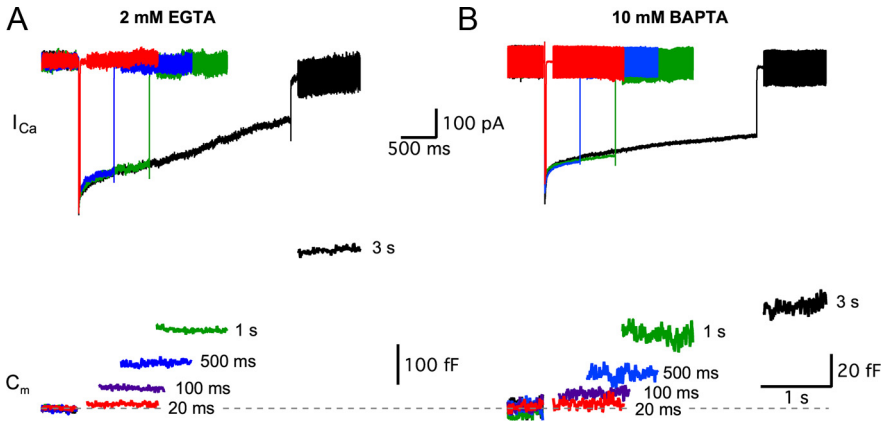

Figure 2. Hair cell Ca^{2+} currents and capacitance changes (ΔC_m). Voltage-clamped hair cells were depolarized from a holding potential of −90 to −30 mV for various durations with 2 mM EGTA (***A***) or with 10 mM BAPTA (***B***) as internal Ca^{2+} buffers. Top panels, Evoked Ca^{2+} currents with 20 ms (red), 500 ms (blue), 1 s (green), and 3 s (black) pulses. Bottom panels, The membrane capacitance (C_m) increases with the duration of the step depolarizing pulse [20 ms (red), 100 ms (purple), 500 ms (blue), 1 s (green), and 3 s (black)]. Note the fivefold difference in vertical scales indicating the greatly reduced exocytosis when 10 mM BAPTA is present in the hair cells. Note also the nearly twofold larger ΔC_m jump for 3 s versus 1 s depolarizing pulses with EGTA, whereas this difference is much smaller with BAPTA. This suggests that 10 mM BAPTA inhibits vesicle recruitment. When 2 mM EGTA is present in the hair cell, we also observed greater Ca^{2+} current inactivation with long depolarizing pulses.

is limited by the rate of Ca^{2+} influx, the slow Ca^{2+}-dependent inactivation component of the Ca^{2+} current (I_{Ca}) during long depolarizing stimuli (Fig. 2*A*) may partially account for the lack of a third subgroup. However, the fast I_{Ca} inactivation was too rapid to account for the distinction between subgroups 1 and 2. Distinct kinetic subgroups with different rates of release suggested that there were functionally distinct vesicle pools. However, determining the size of these putative vesicle pools directly was difficult because the ΔC_m did not plateau (Fig. 3*A*, black data points).

We next attempted to isolate the vesicle pools by restricting the spread of the synaptic Ca^{2+} microdomains with higher concentrations of a slow internal Ca^{2+} buffer (10 mM EGTA; Fig. 3*A*,*B*, red), which may slow down the recruitment rates of vesicles at ribbon synapses (Mennerick and Matthews, 1996; Babai et al., 2010). The first two subgroups then showed clear single-exponential relationships with plateaus in ΔC_m plotted against pulse duration (Fig. 3*B*, red in left and middle panels). The asymptote ($t \rightarrow +\infty$) of the first subgroup (5–50 ms) was 29 fF, and the data were well fit by $\Delta C_m = 29\ \text{fF} \cdot (1 - \exp(-t/\tau))$ with $\tau = 23.4$ ms ($R^2 = 0.99$). The asymptote of the second subgroup (100 ms to 1 s) was 138.7 fF and the average $\Delta C_m = 138.7\ \text{fF} \cdot (1 - \exp(-t/\tau))$ with $\tau = 323$ ms ($R^2 = 0.99$). The third subgroup (1–3 s; Fig. 1*B*, red in right panel) showed a nonsaturating linear relationship with the same slope as in 2 mM EGTA. Surprisingly, we found that 10 mM EGTA did not block the vesicle release significantly except for four data points (50, 100, 500, and 1000 ms; Fig. 3*B*, green asterisks). This contrasts starkly with results from goldfish bipolar cells and mouse inner hair cells in which 5–10 mM EGTA was very effective at blocking the sustained component of exocytosis evoked by long depolarizing pulses (Moser and Beutner, 2000; Coggins and Zenisek, 2009). With 10 mM BAPTA, however, ΔC_m decreased significantly for all data points by 80–90% (Fig. 3*A*,*B*, blue). To confirm that the ΔC_m plateaus with 10 mM EGTA were not due to differences in Ca^{2+} influx, we compared the Ca^{2+} influx charges (integral of I_{Ca}) in 2 and 10 mM EGTA (Fig. 3*D*). The Ca^{2+} charges in 10 mM EGTA were not significantly different from those in 2 mM EGTA for all the depolarizing pulse durations.

Next, we determined the efficacy of exocytosis among the three subgroups identified in Figure 3*B*, calculated as a ratio of the average ΔC_m per Ca^{2+} charge influx (or per number of Ca^{2+} ions) during the depolarizing pulse (Mansvelder and Kits, 1998; Hull et al., 2006). The efficacy for exocytosis was initially high for both 2 mM EGTA (Fig. 3*E*, black) and 10 mM EGTA (Fig. 3*E*,*F*, red) internal solutions, but decreased as depolarization duration increased, presumably due to vesicle pool depletion. With 10 mM EGTA, the efficacy decreased sharply between different subgroups compared with changes within one subgroup (Fig. 3*F*, arrows), suggesting greatly reduced efficacy after depletion of the first pool and a further reduction in efficacy after depletion of the second pool.

Morphological characterization of synaptic vesicle populations

To provide an anatomical correlate for our physiological estimates of vesicle pools, we inventoried synaptic vesicle populations using ultrastructural methods, assuming that the preferential site of exocytosis is located near synaptic ribbons (Zenisek et al., 2000; Zampighi et al., 2011). We first quantified the number and size of ribbon synapses per hair cell by serial section electron microscopy (Fig. 4). Four hair cells from two bullfrogs were entirely sectioned (two examples shown in Fig. 4*A*), and five additional hair cells were partially sectioned from another bullfrog. For our entirely sectioned cells, we counted a mean of 55.5 ribbon synapses per hair cell, a mean ribbon diameter of 208.8 nm, and the CV (a ratio of the SD to the mean) of the mean ribbon diameter at 9.8% (Fig. 4*C*). Additional estimates from the five partially sectioned cells were consistent with these numbers (mean ribbon number, 51.4; mean diameter, 218.7 nm; mean CV, 9.9%). Auditory nerve fibers were also inventoried for three of the entirely sectioned hair cells. These hair cells had a total of 53, 54, and 65 ribbons, and each hair cell had one large claw-like afferent receiving input from 44, 31, and 27 ribbons, respectively (Fig. 4*A*,*B*, brown fiber). Other ribbons appeared to be presynaptic to additional fibers (Fig. 4*B*, green fiber); however, the limited spatial dimensions of our reconstructions made it impossible to determine whether these fibers are distinct or arise from the branching of a shared fiber outside of the reconstructed volume.

In addition, for the two segmented hair cells (shown in Fig. 4*A*), the nearest-neighbor distance between ribbon synapses was calculated in three-dimensional space. A minority of synapses exhibited two ribbons sharing the same active zone (7 of 111 synapses). Treating these ribbon doublets as single ribbon synapses, we found the average distance between ribbon synapses to be 1.71 μm (SD = 0.65) and 1.34 μm (SD = 0.38), similar to the distance measured in mammalian inner hair cells (Meyer et al., 2009). By considering the basolateral membrane surface area at the synaptic pole of the two hair cells where ribbons were counted, we calculated the density of ribbon synapses at 0.158 ribbon synapses/μm^2 and 0.117 ribbon synapses/μm^2. Individual ribbon synapses were thus well separated from each other and may operate as independent units under strong Ca^{2+} buffering conditions (Issa and Hudspeth, 1996).

We next defined the relationship between the diameter of a ribbon and its vesicle pools using serial sections (Fig. 5*A*) and electron tomography (Fig. 5*B*). A total of 34 synapses (22 normal-external Ca^{2+} fixed, 12 zero-external Ca^{2+} fixed) with ribbons of varying diameters were entirely reconstructed and quantified (Fig. 5*C*). In addition to serial section reconstructions, nine ribbon synapses (four normal-Ca^{2+} fixed, five zero-Ca^{2+} fixed) were reconstructed by electron tomography. Each electron tomography reconstruction contained approximately one-half of the associated vesicle pools of the ribbon (mean, 49.2% reconstructed; $n = 9$), allowing us to estimate the full vesicle pools based on the percentage reconstructed.

Polynomial fits of the relationship between synaptic ribbon diameter and the size of vesicle pools (Fig. 5*C*, fit lines) allowed us to estimate whole-cell vesicle pools for our serial sectioned hair cells. For our four fully reconstructed hair cells, the IRP is estimated to be 702 ± 100 (mean ± SD), or 12.6 vesicles per ribbon, and the RAP is estimated to be 4308 ± 613, or 77.6 vesicles per ribbon. Similarly, for our tomography data sets, the average number of vesicles in the IRP was 14.8, with an average of 6.8 vesicles touching the membrane. These results agree well with synaptic ribbon reconstructions from the caudal (high frequency) amphibian papilla of *Rana pipiens* frogs where synaptic ribbons varied from 100 to 300 nm in diameter and had 59–81 attached vesicles (Simmons et al., 1995).

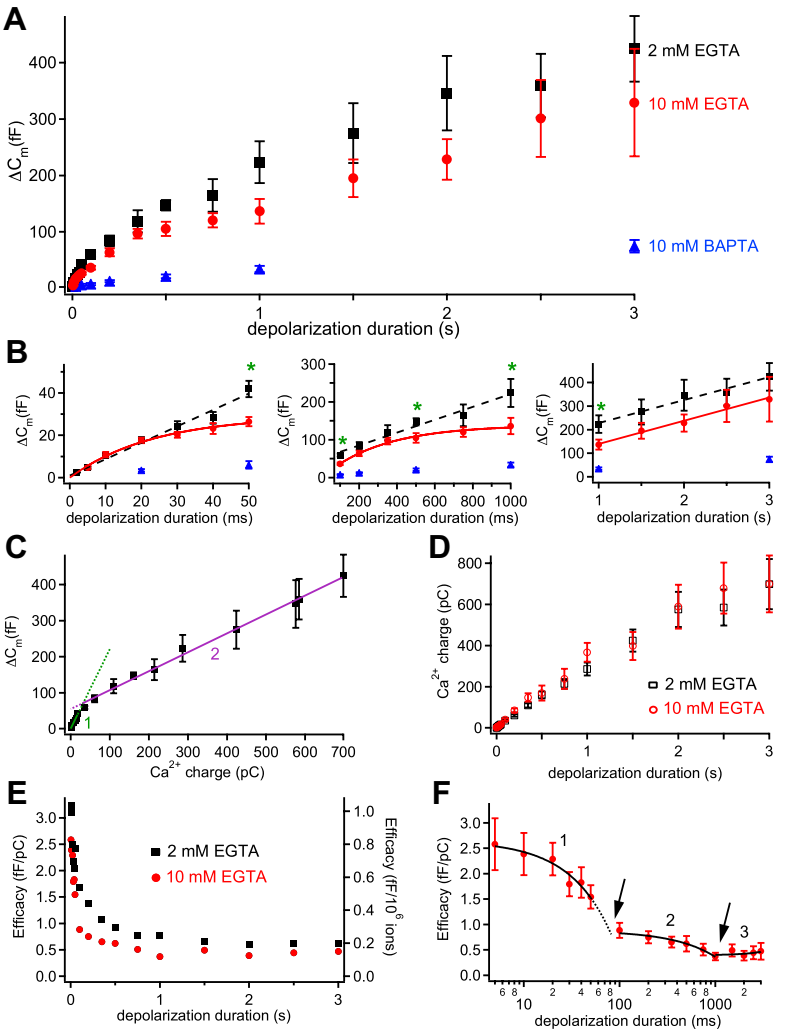

Figure 3. Ca^{2+} buffers and the kinetics of exocytosis from hair cells. Voltage-clamped hair cells were depolarized from a holding potential of −90 to −30 mV for various durations. All data points are expressed as mean ± SEM. ***A***, The relationship between depolarization duration and ΔC_m with various internal hair cell calcium buffer conditions: 2 mM EGTA (black), 10 mM EGTA (red), and 10 mM BAPTA (blue). ***B***, The same data as in ***A*** were divided into three subgroups and plotted separately with best fits. Data with 2 mM EGTA in all plots show linear fits (black dashed lines) with different slopes. The green asterisks reflect significant differences (Student's *t* tests with $p < 0.05$) between 2 mM EGTA and 10 mM EGTA data points. The 10 mM BAPTA decreased ΔC_m significantly for all stimulations ($p < 0.01$; $n = 6–21$). The left figure shows data with 2–50 ms stimuli (subgroup 1). The middle figure shows data with 100 ms to 1 s stimuli (subgroup 2). The right figure shows data with 1–3 s stimuli (subgroup 3). The 10 mM EGTA data show best fit with single exponential function (red) for subgroups 1 and 2 and a linear fit for subgroup 3. ***C***, The relationship between ΔC_m and Ca^{2+} influx charge (integral of the Ca^{2+} current) with 2 mM EGTA in the internal solution. Same data as in ***A*** and ***B***, but now only two straight lines can fit the whole data range. ***D***, The Ca^{2+} influx charge was plotted against depolarizing pulse duration for hair cells dialyzed with 2 mM EGTA (black open squares) or 10 mM EGTA (red open circles). ***E***, The efficacy of exocytosis was calculated from the ratio of ΔC_m divided by Ca^{2+} charge (left axis) or by the number of Ca^{2+} ions that entered the hair cell during the depolarization (right axis) with 2 mM EGTA (black) and 10 mM EGTA (red) internal solutions. The error bars are not included to show the changes of mean values more clearly. ***F***, The efficacy with 10 mM EGTA (same data as in ***E***) was plotted versus depolarizing pulse duration on a semilog scale to show the differential decrease of the efficacy in each group. There are significant drops in the efficacy of exocytosis of subgroups 1 and 2 at the arrows, suggesting that pool depletion reduces exocytosis at these two time points.

The correlation between morphologically and functionally defined vesicle pools

Determining vesicle pool sizes from whole-cell capacitance recordings required an estimate of the capacitance of a single synaptic vesicle. The C_m of a single synaptic vesicle (C_v) in frog saccular hair cells has been reported as 37 aF (vesicle diameter, 34.3) (Lenzi et al., 1999) and has been determined to be 45 aF for bullfrog hair cells from a small sample of vesicles (n = 109 vesicles) (Li et al., 2009). Here, we calculated a C_v of 34 aF ($C_v = \pi d^2 C_s$) using our mean vesicle diameter (d) of 32.9 nm (n = 1467 vesicles; Fig. 5*D*) and a specific membrane capacitance (C_s) of 9 mF/m^2 (Fettiplace et al., 1971; Albillos et al., 1997). Accordingly, the first pool of rapidly releasing vesicles in our physiological recordings, with a size of 29 fF, consisted of ~725–850 vesicles depending on whether C_v = 40 aF (average from previous reports) or 34 aF. This functional estimate of the IRP correlated well with the morphological IRP, which had an average size of 702. The rate of release of this pool was ~0.8 fF/s, or 360–420 vesicles · s^{-1} · ribbon^{-1}. The second pool of vesicles in our recordings (139 fF) consisted of ~3500–4090 vesicles and was released at a slower pace. It correlated well with the morphological RAP, which had an average size of 4308 vesicles. To summarize, our average synaptic ribbon had ~12.6 docked vesicles and a fast releasing pool of 13–15 vesicles that could be completely released by a strong depolarization within ~20–50 ms (Fig. 3*B*). In comparison, frog saccular hair cells have been reported as having a larger synaptic ribbon (diameter of ~400 nm) and a larger pool of 43–66 docked vesicles (Rutherford and Roberts, 2006).

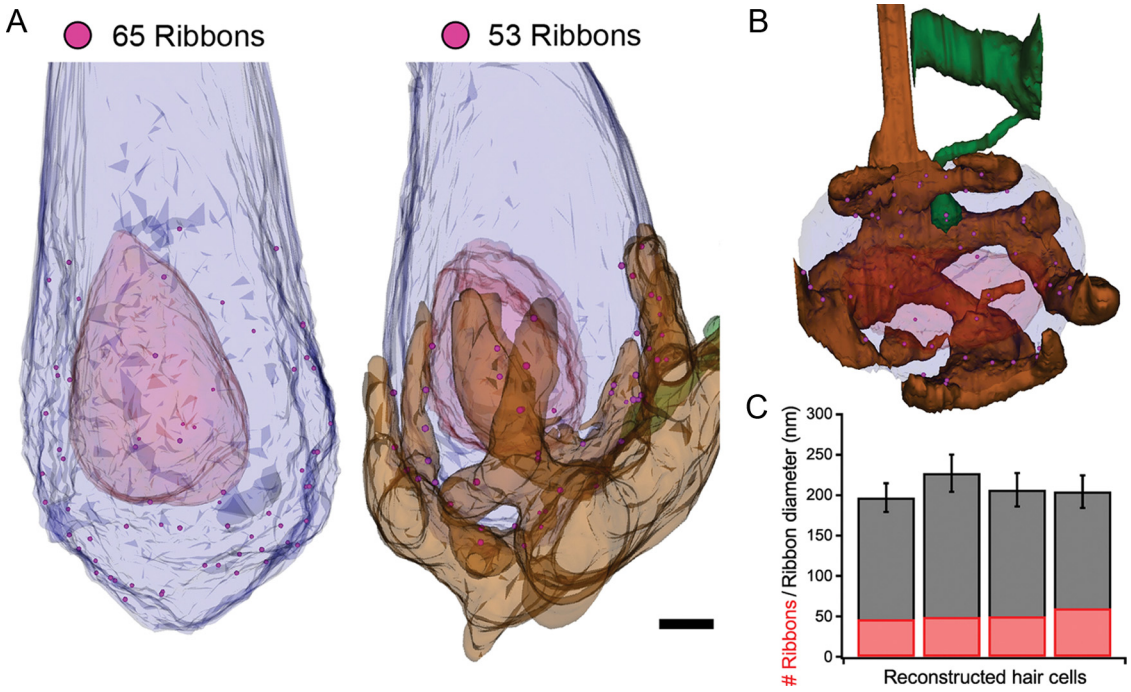

Figure 4. Reconstructions of hair cell ribbon synapse populations and afferent fibers. ***A***, The basal pole of two reconstructed hair cells with 65 and 53 ribbon synapses. The plasma membranes and nuclei of the hair cells are semitransparent blue and red, respectively. Ribbon synapses are shown, to scale, as pink spheres. Proximal afferent fibers terminals were also reconstructed for three hair cells (example at right, semitransparent brown). Scale bar, 2 μm. ***B***, View is looking down onto the basal pole of a hair cell, showing a dominant innervation of the cell from one claw-like, brown fiber. The hair cell had 53 ribbons and 44 contacted the claw-like afferent. All hair cells where fibers were reconstructed showed a similar fiber receiving a majority of the ribbon synapses of the hair cell. A minority of ribbons are presynaptic to *en passant* bouton-like processes (green) extending from trunks of neighboring fibers; however, given our limited reconstruction volume, it is impossible to determine whether these neighboring fibers are ultimately derived from the same fiber. ***C***, The ribbon synapse populations from four hair cells and five partial hair cells were quantified by serial section reconstruction (fully sectioned hair cells shown). The mean number of ribbons is 55.5 with a mean diameter of 209 nm. Error bars indicate SD.

A central difficulty in relating EPSCs to ultrastructure concerns the partially overlapping concepts of the IRP (immediately releasable pool), "docked" vesicles, and vesicles physically touching the presynaptic membrane. Our capacitance recordings (Fig. 3) showed a first wave of rapid release lasting 20–50 ms, presumably allowing IRP vesicles not initially docked (but very close to the membrane) enough time to dock and then release. For the nine tomography data sets used, the average number of vesicles in the <20 nm IRP group was 14.8 (similar in size to the 12.6 vesicles reported from serial section data sets), while the "touching the membrane" IRP group was 6.8. The number of vesicles touching the membrane was therefore sufficient to account for the size of the large multiquantal EPSCs that we observed.

Variability in vesicle size and mEPSC distributions

Our measured vesicle diameter distribution was normally distributed with a mean of 32.9 nm and a CV of 0.110 (Fig. 5*D*). Using EM tomography, Lenzi et al. (1999) reported a CV of 0.261 for synaptic vesicle volumes, noting that for normal vesicle diameter distributions, the CV of vesicle volume: $CV_{vol} = 3 \cdot CV_{diam}$. So our $CV_{vol} = 0.328$, consistent with the CV of single quanta mEPSC amplitudes reported previously for our hair cell synapse (CV = 0.29) (Li et al., 2009). The variability of mEPSC amplitudes may thus originate mostly from the variability of vesicle volumes.

Vesicle mobility and sustained exocytosis

We observed sustained rates of exocytosis of 100 fF/s after 1- to 3-s-long depolarizing pulses (Fig. 3). Assuming a single vesicle capacitance of ~34 aF, this rate of sustained release corresponds to 53 vesicles per second for each of the 55.5 ribbons of the hair cell. Can the rate at which freely diffusing cytoplasmic vesicles hit the ribbon account for this exocytosis rate? If we assume that only diffusion transports vesicles to the synaptic ribbon, where they are immediately released, and we ignore cytoskeletal and plasma membrane barrier effects, the hit rate of vesicles (F) bombarding a spherical ribbon is as follows: $F = 4\pi DRC$, where $D = 1.5 \times 10^{-2}\ \mu m^2\ s^{-1}$ (synaptic vesicle diffusion coefficient) (Holt et al., 2004), $R = 147$ nm (sum of synaptic ribbon radius, 30 nm tethers, and vesicle radius), and C is the concentration of neighboring cytoplasmic vesicles (Jackson, 2006; Rutherford and Roberts, 2008). To estimate the reserve pool of cytoplasmic vesicles at "actively exocytosing" ribbon synapses, five serial section data sets from the "Ca^{2+}-fixed" condition were arbitrarily chosen (see Materials and Methods). The concentration of cytoplasmic vesicles (within ~1 μm of the ribbon) ranged between 2.55 and 4.78% of maximum vesicle packing, averaging 3.65%, so that $C \approx 851$ vesicles/μm^3. We calculate a collision rate of 24 vesicles per second for each ribbon. Diffusion alone, therefore, appears to be inadequate to maintain even the slowest rate of sustained release observed at these synapses. Consequently, an active ATP-dependent, and probably Ca^{2+}-dependent, replenishment mechanism seems to be required to enhance vesicle mobility and concentrate vesicles near synaptic ribbons (Heidelberger et al., 2002).

Physiological estimate of the number of Ca^{2+} channels

To determine the total number of Ca^{2+} channels per hair cell, we used nonstationary noise analysis of Ca^{2+} tail currents (Roberts et al., 1990). Figure 6*A* shows the Ca^{2+} current *I–V* relationship ($n = 5$ cells) (Edmonds et al., 2004). Figure 6*B* shows the voltage-clamp protocol we used to elicited Ca^{2+} tail currents. By plotting

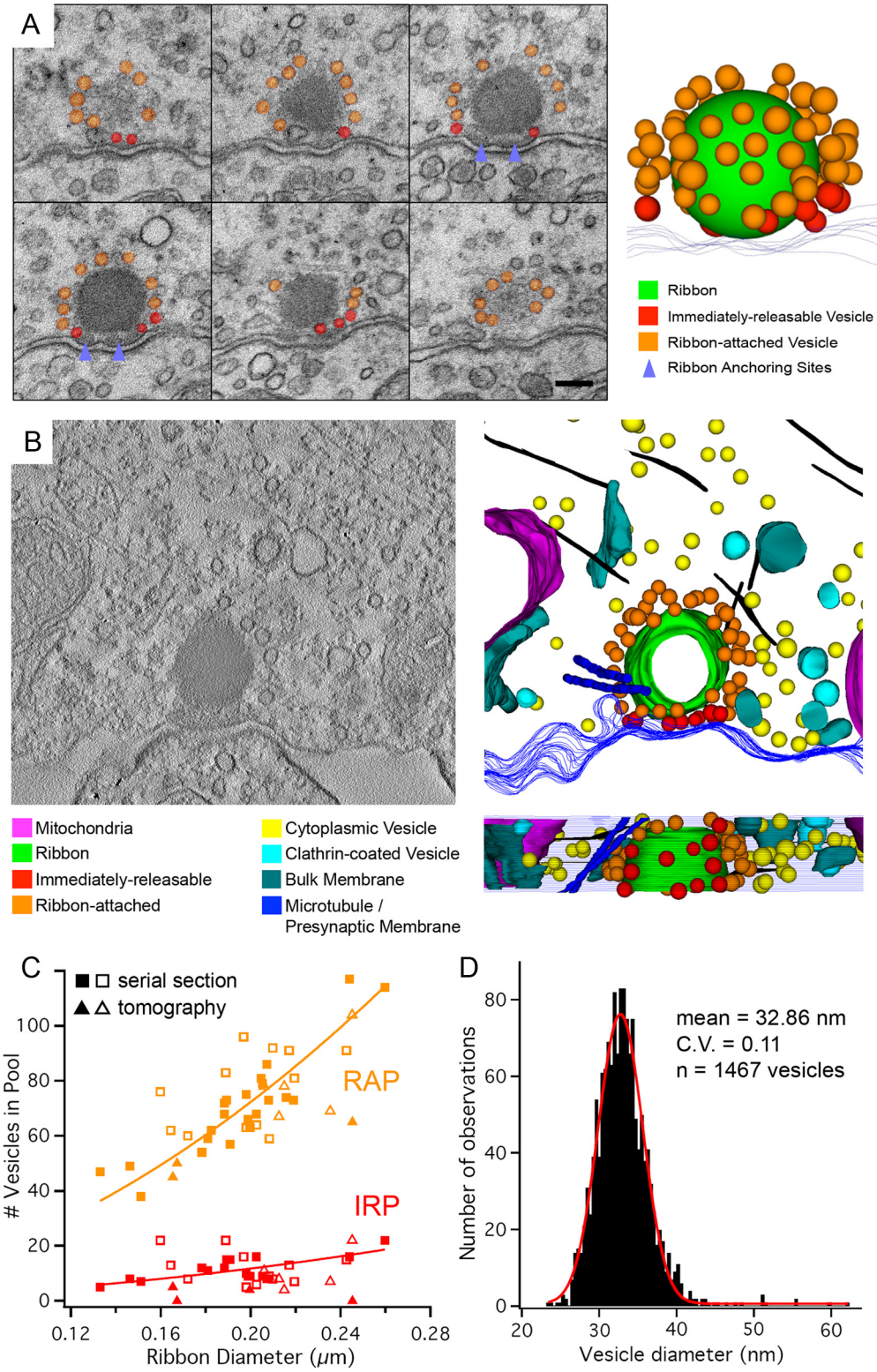

Figure 5. Serial section and electron tomographic reconstruction of ribbon synapse vesicle populations. ***A***, Exemplar set of consecutive 50-nm-thick serial sections imaged at 40,000× and used to reconstruct and count ribbon-associated vesicles. Scale bar, 100 nm. ***B***, The 200 nm-thick sections were used to collect tilt series of projection images, from which tomograms (left) were generated. Subsequent reconstruction of these tomograms (right) provided another means for quantifying anatomical vesicle pools. Clathrin-coated pits and mitochondria were frequently observed near reconstructed ribbons. Microtubules (purple) and actin filaments (black) were also observed, sometimes in close proximity to the ribbon and its vesicle pools. ***C***, A plot of ribbon diameter versus vesicle pool sizes for two fixation methods and two ultrastructural reconstruction methods. The total RAP is orange, while the IRP is in red. Serial section (squares) and electron tomography (triangles) data are displayed for high Ca^{2+} (filled markers) and zero Ca^{2+} (empty markers) fixation conditions. We defined the total ribbon-attached pool as all vesicles <30 nm from the ribbon, and the docked "bottom row" pool as all vesicles <30 nm from the ribbon and also <20 nm from the presynaptic membrane. Because electron tomography provides sufficient resolution to observe vesicles touching the presynaptic membrane (e.g., no gaps), we report this value for the IRP for the tomography data. Because the average ribbon size per cell varies slightly, second-order polynomial fits of our reconstruction data allow us to calculate the estimated vesicle pools for hair cells with ribbons of various sizes. ***D***, The distribution of ribbon-associated vesicle diameters ($n = 1467$ vesicles) has a mean of 32.9 nm (CV = 0.11) and is well fit by a Gaussian function (red).

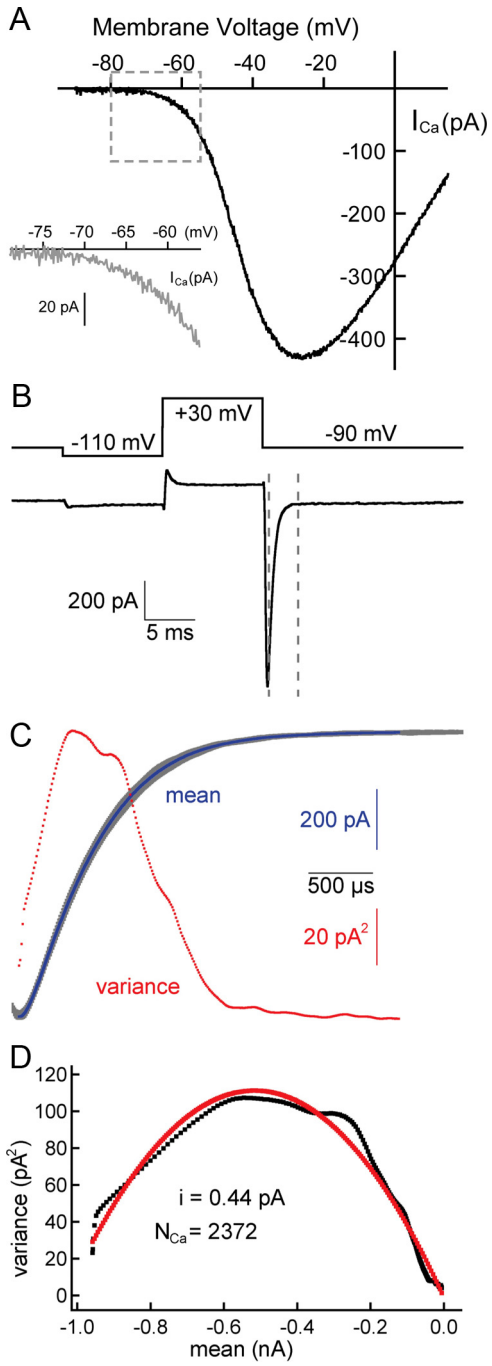

Figure 6. Noise analysis: the number of Ca^{2+} channels and size of single-channel currents. ***A***, The Ca^{2+} current *I–V* relationship for amphibian papilla hair cells after leak subtraction, series resistance compensation (80–90%), and liquid junction potential correction. The Ca^{2+} current (I_{Ca}) begins to activate at approximately −70 mV (inset) and peaks at approximately −30 mV ($n = 5$ cells). ***B***, The hair cell was held at −90 mV, briefly hyperpolarized to −110 mV to relieve any steady-state inactivation, and then depolarized to +30 mV for 10 ms to open all Ca^{2+} channels. A Ca^{2+} tail current (bottom trace) was elicited by repolarizing the hair cell from +30 to −90 mV (top trace) in the presence of the L-type Ca^{2+} channel agonist BayK 8644 (5 μM) and 2 mM external Ca^{2+}. The decay of the tail current between the two dashed lines was used for noise analysis. ***C***, Here, we show 100 superimposed traces (in gray) that were obtained with the same protocol as in ***B***. The mean (in blue) and variance (in red) were calculated on a point-by-point basis. ***D***, The variance was plotted against the mean (in black). The single-channel current (i = 0.44 pA) and the number of Ca^{2+} channels (N_{Ca} = 2372) were estimated by fitting the data to a parabolic function (in red) (see Materials and Methods).

the variance of this tail current against its mean (Fig. 6*C*,*D*), the number of Ca^{2+} channels and their single-channel current was extrapolated by fitting the data with a parabolic function (see Materials and Methods) (Alvarez et al., 2002). We estimated a total number of Ca^{2+} channels $N_{Ca} = 1998 \pm 355$ ($n = 6$ hair cells) and a single-channel current $i = -0.62 \pm 0.19$ pA at −90 mV. Assuming the reversal potential $E_{Ca} = +90$ mV, approximately equal to the thermodynamic E_{Ca}, this yields a single-channel conductance of 3.4 pS. At −30 mV, the peak of the Ca^{2+} current *IV* curve, we calculated that $i = -0.4$ pA. This single-channel current value is very similar to that found in ribbon synapses of inner hair cells and retinal rod bipolar cells (Brandt et al., 2005; Jarsky et al., 2010). Estimates of number of Ca^{2+} channels in mouse inner hair cells and frog saccular hair cells are 1700 and 1800, respectively (Roberts et al., 1990; Brandt et al., 2005).

An alternative method to estimate the number of Ca^{2+} channels uses the resonant frequency of nonmammalian hair cells (Wu and Fettiplace, 1996; Martinez-Dunst et al., 1997). For our amphibian papilla hair cells, at the average steady-state membrane potential $V_{ss} = -49.6 \pm 0.4$ mV, the average resonant or tuning frequency (f_c) was 410 ± 2 Hz ($n = 15$ hair cells), and when $V_{ss} = -54.8 \pm 0.3$ mV, the $f_c = 353 \pm 2$ Hz ($n = 12$). The number of Ca^{2+} channels $N_{Ca} = 2 \cdot (N_{KCa})$ and the number of Ca^{2+}-activated K^+ channels $N_{KCa} = 3.75 \cdot f_c$ (Wu and Fettiplace, 1996). Using this method, we calculate that N_{Ca} varies from 2648 to 3075. We thus estimate from two independent data sets that the number of functional Ca^{2+} channels contained in our hair cells ranges from ~2000 to 3000. Given our average number of 55.5 ribbons per hair cell, we estimate that the average number of Ca^{2+} channels per ribbon is ~40–50, assuming that all hair cell Ca^{2+} channels are clustered near to ribbons (Brandt et al., 2005; Sheets et al., 2011).

Monte Carlo modeling of Ca^{2+} influx and propagation under the synaptic ribbon space

One hypothesis of how multiquantal EPSC events can still occur in 10 mM BAPTA conditions (Fig. 1*B*) is that the restricted, small space available under a synaptic ribbon permits the rapid saturation or depletion of Ca^{2+} buffers near open Ca^{2+} channels (Roberts, 1994). We therefore asked how the kinetics of Ca^{2+} influx and Ca^{2+} buffering influence the local concentration of free Ca^{2+} ions in the crowded space under a synaptic ribbon.

To examine the changes in free Ca^{2+} concentration following the onset of Ca^{2+} channel opening, we used Monte Carlo diffusion simulations incorporating the detailed spatial parameters of our ribbon synapse reconstructions as well as the Ca^{2+} buffer concentrations, channel numbers, and Ca^{2+} currents of our physiology experiments (Fig. 7*A*). To simulate Ca^{2+} currents resulting from a depolarizing pulse from −90 to −30 mV, we opened 22 or 23 Ca^{2+} channels of a total of 45 located under the ribbon (for a Ca^{2+} current of approximately −9 pA, using −0.4 pA as the single Ca^{2+} channel current). Simulations were run in either 2 mM EGTA (Fig. 7*B*) or 10 mM BAPTA (Fig. 7*C*) buffering conditions while monitoring free Ca^{2+} concentration at eight different locations (Fig. 7*A*, red boxes). In 2 mM EGTA conditions, free Ca^{2+} reached stable concentrations rapidly (~100–200 μs; Fig. 7*B*), with the region underneath the ribbon experiencing uniformly large (millimolar) concentrations. However, with increasing distance from the base of the ribbon (and into less encumbered cytoplasmic space), free Ca^{2+} concentrations diminished sharply. Simulations in 10 mM BAPTA conditions (Fig. 7*C*) revealed dramatic reductions in free Ca^{2+} concentrations, particularly around the sides of the ribbon. Although the slower rise of Ca^{2+} with stronger

buffer suggests a longer EPSC latency for our physiological recordings, variability between synapses in the number of open Ca^{2+} channels and size of vesicle pools, along with variable numbers of ribbon synapses per afferent fiber, made analysis of EPSC latency difficult. These simple simulations likely overestimated the local Ca^{2+} concentration near the channels, as we did not take into account the dramatic alterations of the Ca^{2+} electrochemical driving force that such high local Ca^{2+} concentration would cause. However, despite this overestimation, rises in local Ca^{2+} concentrations were still confined to the bottom row of vesicles in 10 mM BAPTA conditions.

Since multivesicular release persisted despite the 10 mM BAPTA presynaptic Ca^{2+} buffering and at relatively low hair cell membrane potentials (Fig. 1*B*), it was not clear how the spatial spread of free Ca^{2+} related to synaptic vesicles when fewer channels were open (Fig. 8). In 2 mM EGTA, large Ca^{2+} microdomains encompassing several vesicles arose from the opening of a single channel. Comparable peak Ca^{2+} concentration could be obtained in 10 mM BAPTA by the opening of six channels. For both of these conditions, we found a dramatic enhancement of the Ca^{2+} microdomain when the ribbon was considered to be an opaque diffusion barrier and restrictor of presynaptic space.

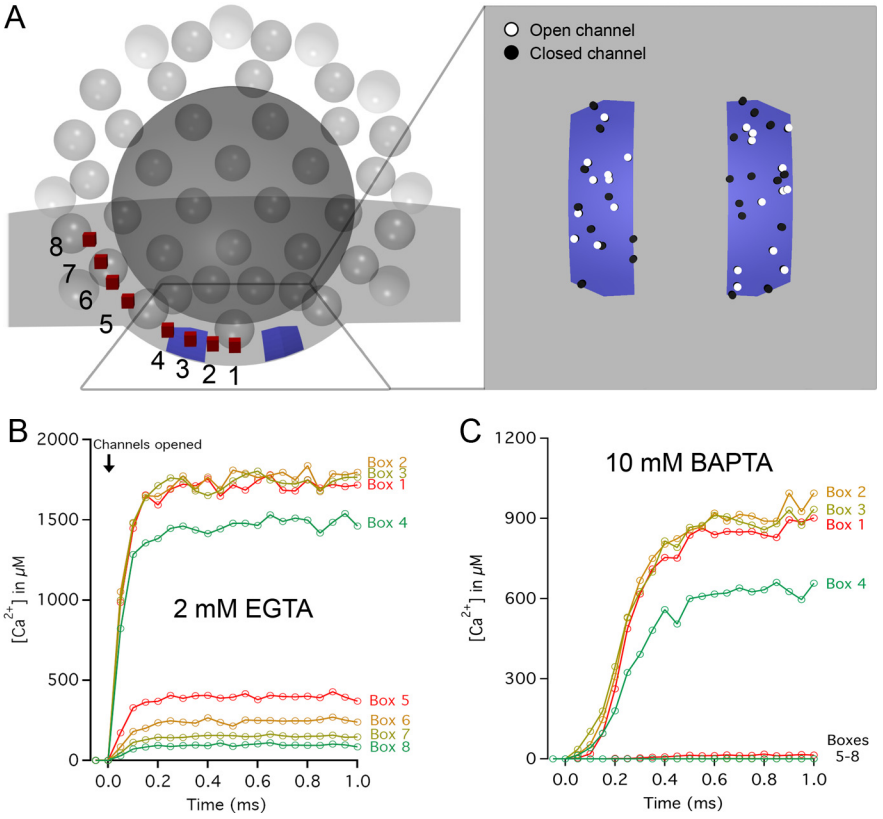

Figure 7. Monte Carlo simulations of Ca^{2+} diffusion near the synaptic ribbon. ***A***, A rendering of a cross-section of the model used for Ca^{2+} influx simulation. Forty-five Ca^{2+} channels were randomly tiled within two stripes of designated presynaptic membrane (blue; see inset for top-down view). To simulate a depolarizing pulse corresponding to a membrane potential of −30 mV, each open channel was given a constant current of −0.4 pA, yielding a synaptic current of approximately −9 pA. The concentration of free Ca^{2+} was monitored every 50 μs at eight locations (10 nm boxes; red) spanning from underneath the ribbon (Box 1) to the second row of synaptic vesicles away from the presynaptic membrane (Box 8). The free Ca^{2+} concentration as a function of time after channel opening is shown for 2 mM EGTA (***B***) and 10 mM BAPTA (***C***) presynaptic Ca^{2+} buffering conditions. A sharp drop in concentration is evident for both conditions across the transition from underneath the ribbon (Boxes 1–4) to the periphery of the ribbon (Boxes 5–8). Data in ***B*** and ***C*** represent the averages of eight simulations run with different random number seeds.

Previously, we described a sharp transition from sparse mEPSC events that are uniquantal (quantal size, −57 pA) to abundant multiquantal EPSC events (amplitudes >100 pA) as hair cells were progressively depolarized during paired recordings [Li et al. (2009), their Fig. 5]. An example of these previous data is shown in Figure 9, *A* and *B*, for hair cells dialyzed with 2 mM EGTA and 10 mM BAPTA, respectively. Note that a small 3 mV increase in hair cell depolarization caused the amplitude of the EPSCs to suddenly increase in size. With 2 mM EGTA, this transition point occurred at approximately −70 mV, where the macroscopic $I_{Ca} < -10$ pA (Fig. 6*A*, inset). From $I_{Ca} = i \cdot P_o \cdot N_{Ca}$ (where $i = -0.54$ pA at −70 mV, $N_{Ca} = 2000$, and P_o is the single-channel open probability), we estimated that $P_o < 0.009$ at −70 mV. With 40–50 Ca^{2+} channels per ribbon, the probability of two or more opening simultaneously to trigger a multiquantal release event was very low. However, with 10 mM BAPTA, the transition to multiquantal EPSC events occurred only at potentials more depolarized than −60 mV, when Ca^{2+} channel open probability was considerably higher. These results suggest that one open Ca^{2+} channel may be sufficient to trigger multivesicular release under weak Ca^{2+} buffering conditions (2 mM EGTA), whereas several Ca^{2+} channels are required to open before a multivesicular release event can occur under strong Ca^{2+} buffering conditions (10 mM BAPTA).

To test the hypothesis that a local depletion of Ca^{2+} buffers by open Ca^{2+} channels underlies the transition to multiquantal EPSC events in 10 mM BAPTA conditions (Fig. 1*B*), we resorted again to our Monte Carlo simulations. We monitored the concentrations of free Ca^{2+} and BAPTA in a 100-nm-diameter region under the ribbon (Fig. 9*C*,*D*), while varying the number of open Ca^{2+} channels. In addition, the same simulations were repeated for three different ribbon models: (1) a model incorporating vesicles numbers consistent with our reconstructions (Fig. 9*E*, black inset); (2) a model incorporating maximum vesicle packing (Fig. 9*E*, red inset); and (3) a model incorporating vesicles numbers consistent with our reconstructions, but where the ribbon was not a barrier to diffusion (Fig. 9*E*, blue inset). For the model closely resembling our reconstructed ribbons, opening less than ~11 channels resulted in relatively modest increase in free Ca^{2+} concentration (Fig. 9*E*, black trace). However, large increases in free Ca^{2+} concentration resulted from opening >11 channels, suggesting a transition point reminiscent of EPSC recordings. Consistent with the idea that tighter packing of ribbon-associated vesicles excludes more presynaptic free volume, thereby reducing local Ca^{2+} buffering capability, the model incorporating maximum vesicle packing showed a shift in the transition point to approximately five channels (Fig. 9*E*, red trace). In contrast, the model lacking a ribbon diffusion barrier showed relatively modest increases in free Ca^{2+} across the entire range of channel openings that were simulated (Fig. 9*E*, blue trace). Our Monte Carlo simulations thus suggest that, by acting as a "diffu-

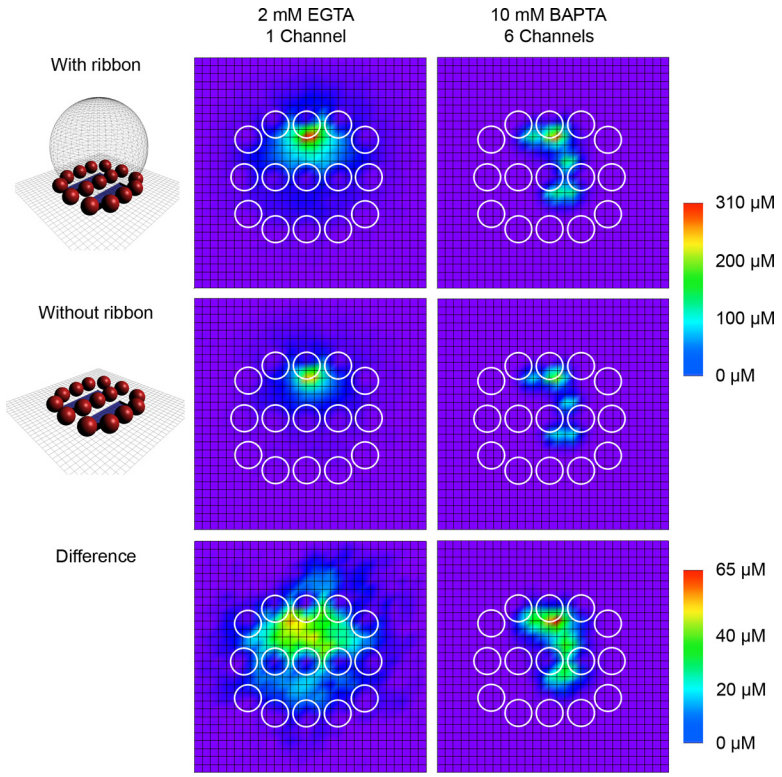

Figure 8. The spatial profile of Ca^{2+} underneath the synaptic ribbon. A separate set of simulations was created to describe the spatial extent of local Ca^{2+} microdomains and the influence of the ribbon. A 30 × 30 grid of 10 nm boxes were used to monitor free Ca^{2+} concentration at the presynaptic membrane surface over time while different numbers of channels were opened. To facilitate the grid design, the ribbon was considered a sphere with a flat cap removed to maintain a flat contact area with the presynaptic membrane. Vesicle outlines are depicted as circles within the grid. Shown are free Ca^{2+} concentrations averaged over 1 ms beginning 5 ms after channel opening. In 2 mM EGTA Ca^{2+} buffering conditions (left column), a single open channel ($i = -0.54$ pA, as expected at $V_m = -70$ mV) resulted in widespread, large free Ca^{2+} nanodomains. The presence of the ribbon as a diffusion barrier and restrictor of space led to an enhancement in Ca^{2+} concentration of tens of micromolar for hundreds of square nanometers. A comparable peak Ca^{2+} concentration was possible in 10 mM BAPTA buffering conditions (right column) by opening six channels ($i = -0.5$ pA, as expected at $V_m = -60$ mV). Although the spatial spread of free Ca^{2+} under 10 mM BAPTA conditions was restricted relative to 2 mM EGTA conditions, the presence of the ribbon as a diffusion barrier remained capable of enhancing Ca^{2+} concentration.

sion barrier" to incoming Ca^{2+} ions, the synaptic ribbon may function as a local Ca^{2+} concentration booster that promotes synchronous multivesicular release.

Discussion

How does one account for the unusually large amplitudes of individual EPSC events at hair cell synapses? One potential explanation is that presynaptic membrane-docked vesicles are released in a coordinated, synchronous fashion. Whether this coordination is mediated by tight colocalization of vesicles with Ca^{2+} channels, by very large presynaptic Ca^{2+} microdomains that might encompass multiple vesicles, or even by mechanical coupling of vesicles remains unclear. Alternatively, large EPSC events could be mediated by the compound fusion and coalescence of several vesicles tethered to the ribbon before the final release event (Parsons and Sterling, 2003; Edmonds et al., 2004). Our results favor a synchronous release mechanism over a two-step compound fusion mechanism in three main ways. First, the kinetics of EPSCs remained fast across presynaptic Ca^{2+} buffering conditions, and even with concentrations of BAPTA that severely restrict the spread of free Ca^{2+} away from the presynaptic membrane. Second, our anatomical and physiological inventories of synaptic vesicle populations in hair cells revealed a close correlation between the population of ribbon-attached vesicles most proximal to the presynaptic membrane and the size of the first, ultrafast wave of vesicle release (Mennerick and Matthews, 1996). Third, our Ca^{2+} diffusion simulations, incorporating the volume-excluding effect of the ribbon and its associated vesicles, demonstrate that small differences in the number of open Ca^{2+} channels may result in large and rapid increases in free Ca^{2+} concentration under the ribbon. As such, the influence of presynaptic structures on Ca^{2+} dynamics at the base of the ribbon may facilitate a synchronous release mechanism and account for the sharp transition to, and fast kinetics of, the large EPSCs.

Compound fusion and EPSCs at hair cell synapses

Recently, compelling EM evidence for compound fusion was presented for strongly stimulated bipolar cell ribbon synapses (Matthews and Sterling, 2008). However, compound fusion at other synapses exhibits large EPSCs with slower rise times compared with mEPSCs (He et al., 2009). Assuming both single and compound vesicles form the same narrow fusion pore with the plasma membrane, the slower rise time of large EPSCs likely results from a compound vesicle requiring more time to fully void its transmitter content than a single synaptic vesicle. Indeed, the amount of glutamate released from a vesicle, C_r in time t is described by the following: $C_r = C_o \cdot [1 - \exp(-t/\tau_v)]$, where C_o is the amount initially in the vesicle, and $\tau_v = VL/(\pi r_o^2 D)$, where V is the vesicle volume, L is the pore length, r_o is the pore radius, and D is the diffusion coefficient of glutamate in the pore (Almers et al., 1991). To account for the fast rise times (<0.2–0.3 ms) of large EPSCs in our experiments, compound fusion would require at least two processes: first, homotypic fusion of vesicles along the upper rows of a ribbon should occur in a Ca^{2+}-independent manner (since these vesicles are located >40–100 nm from Ca^{2+} channels and are bathed by 10 mM BAPTA; Fig. 7); second, to avoid a slow EPSC rise time, Ca^{2+}-dependent exocytosis of a large, compound vesicle should produce a rapidly expanding fusion pore (Stiles et al., 1996). Since synaptic vesicles are not known to fuse with each other in a Ca^{2+}-independent manner, and previous evidence for compound exocytosis does not imply fast fusion pore expansion rates (Van der Kloot and Naves, 1996; He et al., 2009), the classically defined compound fusion mechanism appears implausible for hair cell synapses.

A crowded, dynamic presynaptic space

That the ribbon may serve as a diffusion barrier to Ca^{2+} ions is supported by estimates that a large fraction (>67%) of the volume of the ribbon is occupied by a tightly packed protein called RIBEYE (Zenisek et al., 2004), which constitutes only one of several different protein fractions present in the ribbon (Magu-

palli et al., 2008). This suggests that the dense matrix of proteins forming the ribbon has little, if any, open space to permit free Ca^{2+} diffusion in its interior. Computer modeling of Ca^{2+} influx at frog saccular hair cells demonstrated that a large ribbon (diameter, ~400 nm) that acts as a diffusion barrier causes a dramatic enhancement in the steady-state Ca^{2+} concentration and local depletion of unbound Ca^{2+} buffer in the space between the ribbon and the presynaptic membrane (Roberts, 1994). In addition, docked synaptic vesicles can also act as diffusion barriers that distort the single Ca^{2+} channel nanodomains, resulting in large concentration differences across the surface of the vesicle (Shahrezaei and Delaney, 2004). Combining these two putative diffusion barriers into a single model based on our ultrastructural characterizations, we reach similar conclusions.

Electron tomography of frog sacculus ribbon synapses following inhibition of release in low external Ca^{2+} conditions showed an increase in the vesicle packing density around and underneath the ribbon (Lenzi et al., 2002). For our hair cells, which are held at −90 mV before release, vesicles are likely at higher packing densities as well. Under these conditions, ribbons fully packed with vesicles presumably maximize the release probability of large, fast multivesicular events in several ways: first, minimizing the available volume for Ca^{2+} diffusion serves to maximize the increase in Ca^{2+} concentration for a given Ca^{2+} current; second, multiple docked vesicles in the vicinity of a channel experience this maximized concentration (Fig. 8); and third, the fusion of a vesicle cohort suddenly creates extra diffusional volume at the active zone, temporarily decreasing the release probability until new docked vesicles can repopulate the available space next to the Ca^{2+} channels. Importantly, simulations with 10 mM BAPTA in the cytoplasm reveal that high Ca^{2+} levels exist only near docked vesicles, where unbound BAPTA is severely depleted near open Ca^{2+} channels. Once the BAPTA is depleted, incremental increases in the number of open Ca^{2+} channels can result in large increases in local Ca^{2+}, consistent with the sharp transition from mEPSCs to large EPSCs that we observe across a range of only a few millivolts (Fig. 9*A*). Further studies of the voltage-dependent flicker open probability of single Ca^{2+} channels are needed to better understand this transition from single quanta to multiquantal release (Zampini et al., 2010).

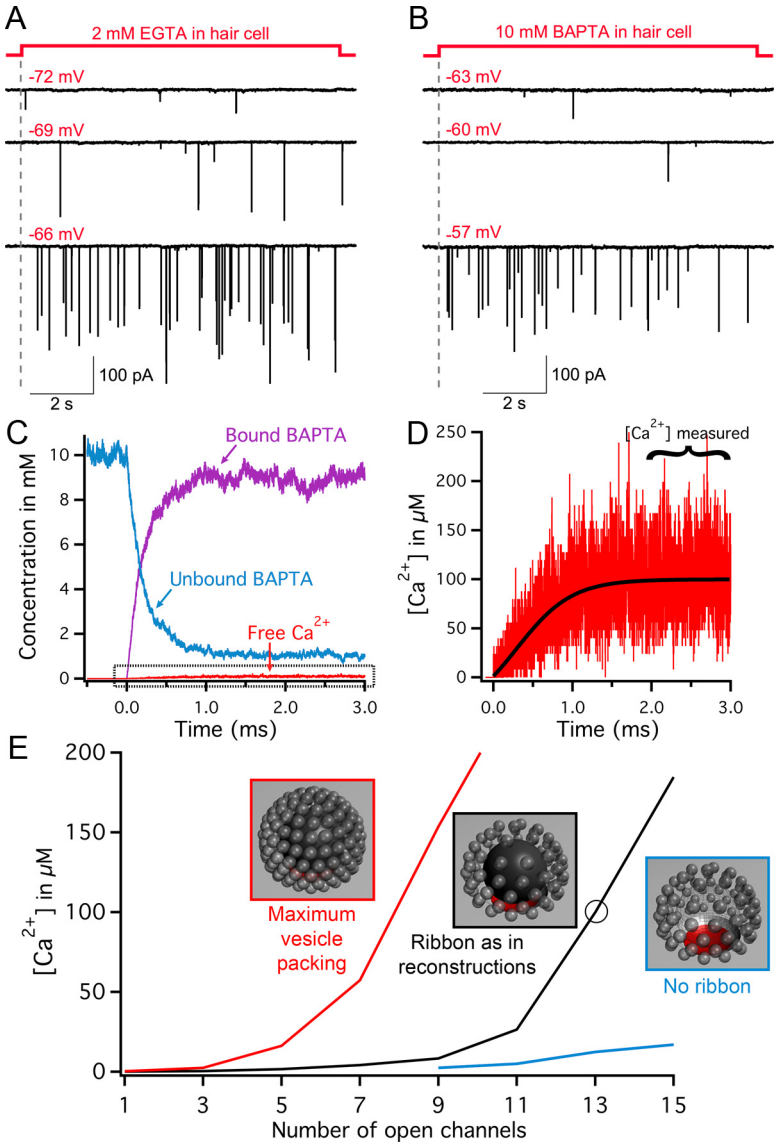

Figure 9. Large multiquantal EPSCs triggered by the opening of few Ca^{2+} channels. ***A***, Paired recordings from a 2 mM EGTA dialyzed hair cell held at −90 mV and depolarized to various membrane potentials in 3 mV increments (shown in red). At −72 mV, only small-amplitude EPSCs are observed (presumably single quanta events). However, a further small depolarization to −69 mV (where I_{Ca} starts to activate) suddenly evokes large-amplitude EPSCs, which become more frequent with further depolarization to −66 mV. ***B***, Paired recordings from a 10 mM BAPTA dialyzed hair cell held at −90 mV and depolarized to various membrane potentials (red). At −63 and −60 mV, only small-amplitude EPSCs are observed (presumably single quanta events). However, a further small depolarization to −57 mV suddenly evokes large-amplitude EPSCs [***A*** and ***B*** modified from the study by Li et al. (2009)]. ***C–E***, Monte Carlo simulations of Ca^{2+} buffer concentration and free Ca^{2+} concentration for the region underneath the synaptic ribbon after opening Ca^{2+} channels ($i = -0.5$ pA, as expected at $V_m = -60$ mV). Simulations were run on three separate ribbon models with different vesicle packing or restriction of free space (models shown in insets of ***E***). ***C*** and ***D*** show simulation data from the opening of 13 channels (circled point on black trace in ***E***). Note the rapid decrease in the 10 mM unbound BAPTA and symmetric increase in bound BAPTA to near 10 mM levels. The free Ca^{2+} concentration rises as unbound BAPTA is depleted. ***D***, The boxed area of ***C*** is expanded, showing the rise in average Ca^{2+} to levels near 100 μM. The Ca^{2+} concentration in all simulations was measured by averaging the concentration for 1 ms beginning 2 ms after channel opening. ***E***, Simulation results are shown for three ribbon models with 10 mM BAPTA. The Ca^{2+} concentrations are plotted versus the number of open Ca^{2+} channels for a ribbon model representative of our synapse reconstructions (same size and vesicle populations; black trace); the same model but with maximal vesicle packing (red trace); a model incorporating vesicles numbers representative of our reconstructions, but with a ribbon that is not a barrier to diffusion (blue trace).

At the cellular level, enhancement of local Ca^{2+} concentrations by ribbons with full pools of docked vesicles might account for our observations of initially high efficacy of exocytosis, decaying dramatically with depletion of the releasable pool (Fig. 3*F*). Accordingly, experiments using the flash photolysis of caged-Ca^{2+} in bipolar and inner hair cells show that the fast component (rise time, <1 ms) of exocytosis requires large elevations of pre-

synaptic Ca^{2+} to ~100 μM (Heidelberger et al., 1994; Beutner et al., 2001). Our *in vitro* recordings and *in silico* simulations thus suggest that docked vesicle fusions mediate the large and fast EPSC events. Furthermore, the rate-limiting step for ongoing release during continuous hair cell stimulation may not be exocytosis itself, but the Ca^{2+}-dependent recovery rate from depletion of the vesicle pool docked underneath the synaptic ribbon (Furukawa et al., 1982; Cho et al., 2011; Schnee et al., 2011).

Vesicles pools and synaptic ribbon geometry

Recent work has begun to reveal some major differences between ribbon synapses of different sensory neurons (LoGiudice and Matthews, 2009). For instance, the large sheet-like ribbons of cone photoreceptor terminals are capable of acting as "capacitors" that release a large bout of vesicles after being fully "charged" with vesicles in hyperpolarized conditions (Jackman et al., 2009). The synaptic ribbon of retinal bipolar cells is a relatively small plate-like structure, so vesicles do not dock underneath the ribbon, but along its lateral ridge. Accordingly, only 30% of spontaneous EPSCs are multivesicular, and these have a quantal content of only two vesicles (Singer et al., 2004; Jarsky et al., 2010). In contrast, the majority of the spontaneous EPSCs at bullfrog and rat inner hair cells are multiquantal (Li et al., 2009; Grant et al., 2010). Unlike mammalian inner hair cells where a single ribbon synapse apposes a single, dedicated afferent fiber, our afferent fiber reconstructions indicate that dozens of ribbon synapses often feed into a single claw-like afferent fiber (Fig. 4*B*). Is there a functional advantage to this arrangement? One idea originates from the finding that a pool of docked vesicles tightly coupled to the Ca^{2+} channel cluster beneath the ribbon reduces first spike latency and jitter in the auditory nerve (Buran et al., 2010; Frank et al., 2010). Likewise, a large pool of docked vesicles distributed among dozens of ribbon synapses with perhaps different release probabilities may account for the extremely short spike latency and low jitter of some frog afferent fibers (Wittig and Parsons, 2008). Moreover, we argue that, after a large EPSC event, the synaptic ribbon may become refractory to release until it is fully loaded again, so an afferent fiber with multiple ribbon synapses may be better able to sustain a prolonged high rate of large EPSC events. We thus propose that the coordination of several docked vesicles underneath a spherical ribbon endows hair cell synapses with an unmatched ability for large and fast-rising EPSC events that are well suited to trigger phase-locked spikes at high stimulation frequencies.

References

Albillos A, Dernick G, Horstmann H, Almers W, Alvarez de Toledo G, Lindau M (1997) The exocytotic event in chromaffin cells revealed by patch amperometry. Nature 389:509–512.

Almers W, Breckenridge LJ, Iwata A, Lee AK, Spruce AE, Tse FW (1991) Millisecond studies of single membrane fusion events. Ann N Y Acad Sci 635:318–327.

Alvarez O, Gonzalez C, Latorre R (2002) Counting channels: a tutorial guide on ion channel fluctuation analysis. Adv Physiol Educ 26:327–341.

Babai N, Bartoletti TM, Thoreson WB (2010) Calcium regulates vesicle replenishment at the cone ribbon synapse. J Neurosci 30:15866–15877.

Beutner D, Voets T, Neher E, Moser T (2001) Calcium dependence of exocytosis and endocytosis at the cochlear inner hair cell afferent synapse. Neuron 29:681–690.

Bortolozzi M, Lelli A, Mammano F (2008) Calcium microdomains at presynaptic active zones of vertebrate hair cells unmasked by stochastic deconvolution. Cell Calcium 44:158–168.

Brandt A, Khimich D, Moser T (2005) Few $Ca_V1.3$ channels regulate the exocytosis of a synaptic vesicle at the hair cell ribbon synapse. J Neurosci 25:11577–11585.

Buran BN, Strenzke N, Neef A, Gundelfinger ED, Moser T, Liberman MC (2010) Onset coding is degraded in auditory nerve fibers from mutant mice lacking synaptic ribbons. J Neurosci 30:7587–7597.

Bucurenciu I, Kulik A, Schwaller B, Frotscher M, Jonas P (2008) Nanodomain coupling between Ca^{2+} channels and Ca^{2+} sensors promotes fast and efficient transmitter release at a cortical GABAergic synapse. Neuron 57:536–545.

Castorph S, Riedel D, Arleth L, Sztucki M, Jahn R, Holt M, Salditt T (2010) Structure parameters of synaptic vesicles quantified by small-angle X-ray scattering. Biophys J 98:1200–1208.

Cho S, Li GL, von Gersdorff H (2011) Recovery from short-term depression and facilitation is ultrafast and Ca^{2+} dependent at auditory hair cell synapses. J Neurosci 31:5682–5692.

Coggins M, Zenisek D (2009) Evidence that exocytosis is driven by calcium entry through multiple calcium channels in goldfish retinal bipolar cells. J Neurophysiol 101:2601–2619.

Crawford AC, Fettiplace R (1980) The frequency selectivity of auditory nerve fibres and hair cells in the cochlea of the turtle. J Physiol 306:79–125.

Crawford AC, Fettiplace R (1981) An electrical tuning mechanism in turtle cochlear hair cells. J Physiol 312:377–412.

Czech J, Dittrich M, Stiles JR (2009) Rapid creation, Monte Carlo simulation, and visualization of realistic 3D cell models. In: Methods in molecular biology, Systems biology, Vol 500 (Maly IV, ed), pp 237–287. Clifton, NJ: Humana.

Edmonds BW, Gregory FD, Schweizer FE (2004) Evidence that fast exocytosis can be predominantly mediated by vesicles not docked at active zones in frog saccular hair cells. J Physiol 560:439–450.

Fettiplace R, Andrews DM, Haydon DA (1971) The thickness, composition and structure of some lipid bilayers and natural membranes. J Membr Biol 5:277–296.

Fiala JC (2005) Reconstruct: a free editor for serial section microscopy. J Microsc 218:52–61.

Fox AP, Nowycky MC, Tsien RW (1987) Single-channel recordings of three types of calcium channels in chick sensory neurons. J Physiol 394:173–200.

Frank T, Rutherford MA, Strenzke N, Neef A, Pangrsic T, Khimich D, Fetjova A, Gundelfinger ED, Liberman MC, Harke B, Bryan KE, Lee A, Egner A, Riedel D, Moser T (2010) Bassoon and the synaptic ribbon organize Ca^{2+} channels and vesicles to add release sites and promote refilling. Neuron 68:724–738.

Furukawa T, Kuno M, Matsuura S (1982) Quantal analysis of a decremental response at hair cell-afferent fibre synapses in the goldfish sacculus. J Physiol 322:181–195.

Gillis KD (2000) Admittance-based measurement of membrane capacitance using the EPC-9 patch-clamp amplifier. Pflügers Arch 439:655–664.

Glowatzki E, Fuchs PA (2002) Transmitter release at the hair cell ribbon synapse. Nat Neurosci 5:147–154.

Goutman JD, Glowatzki E (2007) Time course and calcium dependence of transmitter release at a single ribbon synapse. Proc Natl Acad Sci U S A 104:16341–16346.

Grant L, Yi E, Glowatzki E (2010) Two modes of release shape the postsynaptic response at the inner hair cell ribbon synapse. J Neurosci 30:4210–4220.

Hallermann S, Pawlu C, Jonas P, Heckmann M (2003) A large pool of releasable vesicles in a cortical glutamatergic synapse. Proc Natl Acad Sci U S A 100:8975–8980.

He L, Xue L, Xu J, McNeil BD, Bai L, Melicoff E, Adachi R, Wu LG (2009) Compound vesicle fusion increases quantal size and potentiates synaptic transmission. Nature 459:93–97.

Heidelberger R, Heinemann C, Neher E, Matthews G (1994) Calcium dependence of the rate of exocytosis in a synaptic terminal. Nature 371:513–515.

Heidelberger R, Sterling P, Matthews G (2002) Roles of ATP in synaptic vesicle pool depletion and replenishment. J Neurophysiol 88:98–106.

Holt M, Cooke A, Neef A, Lagnado L (2004) High mobility of vesicles supports continuous exocytosis at a ribbon synapse. Curr Biol 14:173–183.

Hull C, Studholme K, Yazulla S, von Gersdorff H (2006) Diurnal changes in exocytosis and the number of synaptic ribbons at active zones of an ON-type bipolar cell terminal. J Neurophysiol 96:2025–2033.

Issa NP, Hudspeth AJ (1996) The entry and clearance of Ca^{2+} at individual

presynaptic active zones of hair cells from the bullfrog's sacculus. Proc Natl Acad Sci U S A 93:9527–9532.
Jackman SL, Choi SY, Thoreson WB, Rabl K, Bartoletti TM, Kramer RH (2009) Role of the synaptic ribbon in transmitting the cone light response. Nat Neurosci 12:303–310.
Jackson MB (2006) Molecular and cellular biophysics, p 198. Cambridge, UK: Cambridge UP.
Jarsky T, Tian M, Singer JH (2010) Nanodomain control of exocytosis is responsible for the signaling capability of a retinal ribbon synapse. J Neurosci 30:11885–11895.
Johnson SL, Forge A, Knipper M, Münkner S, Marcotti W (2008) Tonotopic variation in the calcium dependence of neurotransmitter release and vesicle pool replenishment at mammalian auditory ribbon synapses. J Neurosci 28:7670–7678.
Keen EC, Hudspeth AJ (2006) Transfer characteristics of the hair cell's afferent synapse. Proc Natl Acad Sci U S A 103:5537–5542.
Kremer JR, Mastronarde DN, McIntosh JR (1996) Computer visualization of three-dimensional image data using IMOD. J Struct Biol 116:71–76.
Lenzi D, Runyeon JW, Crum J, Ellisman MH, Roberts WM (1999) Synaptic vesicle populations in saccular hair cells reconstructed by electron tomography. J Neurosci 19:119–132.
Lenzi D, Crum J, Ellisman MH, Roberts WM (2002) Depolarization redistributes synaptic membrane and creates a gradient of vesicles on the synaptic body at a ribbon synapse. Neuron 36:649–659.
Lewis ER, Leverenz EL, Koyama H (1982) The tonotopic organization of the bullfrog amphibian papilla, an auditory organ lacking a basilar membrane. J Comp Physiol A Neuroethol Sens Neural Behav Physiol 145:437–445.
Li GL, Keen E, Andor-Ardó D, Hudspeth AJ, von Gersdorff H (2009) The unitary event underlying multiquantal EPSCs at a hair cell's ribbon synapse. J Neurosci 29:7558–7568.
Lindau M, Neher E (1988) Patch-clamp techniques for time-resolved capacitance measurements in single cells. Pflügers Arch 411:137–146.
LoGiudice L, Matthews G (2009) The role of ribbons at sensory synapses. Neuroscientist 15:380–391.
Magupalli VG, Schwarz K, Alpadi K, Natarajan S, Seigel GM, Schmitz F (2008) Multiple RIBEYE-RIBEYE interactions create a dynamic scaffold for the formation of synaptic ribbons. J Neurosci 28:7954–7967.
Mansvelder HD, Kits KS (1998) The relation of exocytosis and rapid endocytosis to calcium entry evoked by short repetitive depolarizing pulses in rat melanotropic cells. J Neurosci 18:81–92.
Martinez-Dunst C, Michaels RL, Fuchs PA (1997) Release sites and calcium channels in hair cells of the chick's cochlea. J Neurosci 17:9133–9144.
Matthews G, Sterling P (2008) Evidence that vesicles undergo compound fusion on the synaptic ribbon. J Neurosci 28:5403–5411.
Mennerick S, Matthews G (1996) Ultrafast exocytosis elicited by calcium currents in synaptic terminals of retinal bipolar neurons. Neuron 17:1241–1249.
Meyer AC, Frank T, Khimich D, Hoch G, Riedel D, Chapochnikov NM, Yarin YM, Harke B, Hell SW, Egner A, Moser T (2009) Tuning of synapse number, structure and function in the cochlea. Nat Neurosci 12:444–453.
Moser T, Beutner D (2000) Kinetics of exocytosis and endocytosis at the cochlear inner hair cell afferent synapse of the mouse. Proc Natl Acad Sci U S A 97:883–888.
Pangrsic T, Lasarow L, Reuter K, Takago H, Schwander M, Riedel D, Frank T, Tarantino LM, Bailey JS, Strenzke N, Brose N, Müller U, Reisinger E, Moser T (2010) Hearing requires otoferlin-dependent efficient replenishment of synaptic vesicles in hair cells. Nat Neurosci 13:869–876.
Parekh AB (2008) Ca^{2+} microdomains near plasma membrane Ca^{2+} channels: impact on cell function. J Physiol 586:3043–3054.
Parsons TD, Sterling P (2003) Synaptic ribbon: conveyor belt or safety belt? Neuron 37:379–382.
Parsons TD, Lenzi D, Almers W, Roberts WM (1994) Calcium-triggered exocytosis and endocytosis in an isolated presynaptic cell: capacitance measurements in saccular hair cells. Neuron 13:875–883.
Pitchford S, Ashmore JF (1987) An electrical resonance in hair cells of the amphibian papilla of the frog *Rana temporaria.* Hear Res 27:75–83.
Ress D, Harlow ML, Schwarz M, Marshall RM, McMahan UJ (1999) Automatic acquisition of fiducial markers and alignment of images in tilt series for electron tomography. J Electron Microsc (Tokyo) 48:277–287.
Roberts WM (1994) Localization of calcium signals by a mobile calcium buffer in frog saccular hair cells. J Neurosci 14:3246–3262.
Roberts WM, Jacobs RA, Hudspeth AJ (1990) Colocalization of ion channels involved in frequency selectivity and synaptic transmission at presynaptic active zones of hair cells. J Neurosci 10:3664–3684.
Roux I, Safieddine S, Nouvian R, Grati M, Simmler MC, Bahloul A, Perfettini I, Le Gall M, Rostaing P, Hamard G, Triller A, Avan P, Moser T, Petit C (2006) Otoferlin, defective in a human deafness form, is essential for exocytosis at the auditory ribbon synapse. Cell 127:277–289.
Rutherford MA, Roberts WM (2006) Frequency selectivity of synaptic exocytosis in frog saccular hair cells. Proc Natl Acad Sci U S A 103:2898–2903.
Rutherford MA, Roberts WM (2008) Afferent synaptic mechanisms. In: The senses: a comprehensive reference, Vol 3 (Dallos P, Oertel D, eds), pp 365–395. New York: Elsevier.
Schnee ME, Ricci AJ (2003) Biophysical and pharmacological characterization of voltage-gated calcium currents in turtle auditory hair cells. J Physiol 549:697–717.
Schnee ME, Santos-Sacchi J, Castellano-Muñoz M, Kong JH, Ricci AJ (2011) Calcium-dependent synaptic vesicle trafficking underlies indefatigable release at the hair cell afferent fiber synapse. Neuron 70:326–338.
Shahrezaei V, Delaney KR (2004) Consequences of molecular-level Ca^{2+} channel and synaptic vesicle colocalization for the Ca^{2+} microdomain and neurotransmitter exocytosis: a Monte Carlo study. Biophys J 87:2352–2364.
Sheets L, Trapani JG, Mo W, Obholzer N, Nicolson T (2011) Ribeye is required for presynaptic $Ca_v1.3a$ channel localization and afferent innervation of sensory hair cells. Development 138:1309–1319.
Simmons DD, Bertolotto C, Leong M (1995) Synaptic ultrastructure within the amphibian papilla of *Rana pipiens pipiens*: rostrocaudal differences. Aud Neurosci 1:183–193.
Singer JH, Lassová L, Vardi N, Diamond JS (2004) Coordinated multivesicular release at a mammalian ribbon synapse. Nat Neurosci 7:826–833.
Smotherman MS, Narins PM (2000) Hair cells, hearing and hopping: a field guide to hair cell physiology in the frog. J Exp Biol 203:2237–2246.
Stiles JR, Bartol TM (2001) Monte Carlo methods for simulating realistic synaptic microphysiology using MCell. In: Computational neuroscience: realistic modeling for experimentalists (De Schutter E, ed), pp 87–127. Boca Raton, FL: CRC.
Stiles JR, Van Helden D, Bartol TM Jr, Salpeter EE, Salpeter MM (1996) Miniature endplate current rise times <100 μs from improved dual recordings can be modeled with passive acetylcholine diffusion from a synaptic vesicle. Proc Natl Acad Sci U S A 93:5747–5752.
Van der Kloot W, Naves LA (1996) Accounting for the shapes and size distributions of miniature endplate currents. Biophys J 70:2175–2184.
von Gersdorff H, Matthews G (1994) Dynamics of synaptic vesicle fusion and membrane retrieval in synaptic terminals. Nature 367:735–739.
von Gersdorff H, Vardi E, Matthews G, Sterling P (1996) Evidence that vesicles on the synaptic ribbon of retinal bipolar neurons can be rapidly released. Neuron 16:1221–1227.
Wittig JH Jr, Parsons TD (2008) Synaptic ribbon enables temporal precision of hair cell afferent synapse by increasing the number of readily releasable vesicles: a modeling study. J Neurophysiol 100:1724–1739.
Wu YC, Fettiplace R (1996) A developmental model for generating frequency maps in the reptilian and avian cochleas. Biophys J 70:2557–2570.
Zampighi GA, Schietroma C, Zampighi LM, Woodruff M, Wright EM, Brecha NC (2011) Conical tomography of a ribbon synapse: structural evidence for vesicle fusion. PLoS One 6:e16944.
Zampini V, Johnson SL, Franz C, Lawrence ND, Münkner S, Engel J, Knipper M, Magistretti J, Masetto S, Marcotti W (2010) Elementary properties of $Ca_V1.3$ Ca^{2+} channels expressed in mouse cochlear inner hair cells. J Physiol 588:187–199.
Zenisek D, Steyer JA, Almers W (2000) Transport, capture and exocytosis of single synaptic vesicles at active zones. Nature 406:849–854.
Zenisek D, Horst NK, Merrifield C, Sterling P, Matthews G (2004) Visualizing synaptic ribbons in the living cell. J Neurosci 24:9752–9759.